Monthly Notices of the ROYAL ASTRONOMICAL SOCIETY

MNRAS **506,** 4321–4343 (2021) https://doi.org/10.1093/mnras/stab1951
Advance Access publication 2021 July 14

Evidence for sub-Chandrasekhar Type Ia supernovae from the last major merger

Jason L. Sanders [1]★ Vasily Belokurov [2] and Kai T. F. Man[2]

[1]*Department of Physics and Astronomy, University College London, London WC1E 6BT, UK*
[2]*Institute of Astronomy, University of Cambridge, Madingley Rise, Cambridge CB3 0HA, UK*

Accepted 2021 July 5. Received 2021 July 5; in original form 2021 May 10

ABSTRACT

We investigate the contribution of sub-Chandrasekhar mass Type Ia supernovae to the chemical enrichment of the *Gaia* Sausage galaxy, the progenitor of a significant merger event in the early life of the Milky Way. Using a combination of data from Nissen & Schuster, the GALactic Archaeology with HERMES (GALAH) Data Release 3 [with 1D non-local thermal equilibrium (NLTE) abundance corrections], and the Apache Point Observatory Galactic Evolution Experiment (APOGEE) Data Release 16, we fit analytic chemical evolution models to a nine-dimensional chemical abundance space (Fe, Mg, Si, Ca, Cr, Mn, Ni, Cu, and Zn) in particular focusing on the iron-peak elements, Mn and Ni. We find that low [Mn/Fe] ~ -0.15 dex and low [Ni/Fe] ~ -0.3 dex Type Ia yields are required to explain the observed trends beyond the [α/Fe] knee of the *Gaia* Sausage (approximately at [Fe/H] $= -1.4$ dex). Comparison to theoretical yield calculations indicates a significant contribution from sub-Chandrasekhar mass Type Ia supernovae in this system (from $\sim$60 per cent to 100 per cent depending on the theoretical model with an additional $\pm$10 per cent systematic from NLTE corrections). We compare to results from other Local Group environments including dwarf spheroidal galaxies, the Magellanic Clouds, and the Milky Way's bulge, finding the Type Ia [Mn/Fe] yield must be metallicity dependent. Our results suggest that sub-Chandrasekhar mass channels are a significant, perhaps even dominant, contribution to Type Ia supernovae in metal-poor systems, whilst more metal-rich systems could be explained by metallicity-dependent sub-Chandrasekhar mass yields, possibly with additional progenitor mass variation related to star formation history, or an increased contribution from Chandrasekhar mass channels at higher metallicity.

Key words: nuclear reactions, nucleosynthesis, abundances – supernovae: general – Galaxy: abundances – Galaxy: evolution.

1 INTRODUCTION

The progenitors of Type Ia supernovae (SNe Ia) are not well understood. Despite this, there has been great success in their use as standard candles for measuring the accelerating expansion of the Universe (Riess et al. 1998; Perlmutter et al. 1999). This has been possible due to empirical relations between luminosity and light-curve decay rate allowing for accurate calibration of their standard candle nature (e.g. Pskovskii 1977; Phillips 1993). However, the cause of such a relation is unclear. There is a growing zoo of different subclasses of observed SNe Ia, indicating a range of formation channels. The commonality between most observed SNe Ia is they likely arise from the explosion of a carbon–oxygen (CO) white dwarf (WD) in a binary system (Whelan & Iben 1973; Iben & Tutukov 1984; Webbink 1984). Beyond this, there are many suggested scenarios for the nature of the progenitor systems and the explosion mechanisms (see the reviews of Hillebrandt & Niemeyer 2000; Maoz, Mannucci & Nelemans 2014; Seitenzahl & Townsley 2017; Ruiter 2020).

The two leading theories for the progenitors of normal SNe Ia are the single- and double-degenerate scenarios. Single-degenerate progenitor systems are mostly anticipated to produce explosions near the Chandrasekhar mass ($M_{\rm Ch}$), whilst double-degenerate systems can produce explosions well below the Chandrasekhar mass (sub-$M_{\rm Ch}$). In the single-degenerate scenario, a CO WD typically accretes from a non-degenerate H-rich companion (non-degenerate He donors are also possible and at low accretion rates could resemble the double-degenerate scenario described below) until the WD approaches the Chandrasekhar mass (Whelan & Iben 1973). At first, the WD enters a turbulent low-level carbon-burning phase lasting a few hundred to a thousand years, which eventually ignites the dynamical burning of carbon. Early models of this scenario (Arnett 1969) considered a supersonic detonation which failed to produce the intermediate-mass elements (e.g. Si) observed in SNe Ia remnants due to the high central density of the WD (Arnett, Truran & Woosley 1971). To remedy this, typically a deflagration flame is initialized which propagates subsonically and causes the WD to expand, producing regions of low density (Nomoto, Thielemann & Yokoi 1984). Eventually, the deflagration flame transitions to a detonation wave leading to the production of intermediate-mass elements in the new lower density regions, and crucially suppressing the production of neutron-rich species (e.g. ^{58}Ni) which are overproduced in pure deflagration models (Khokhlov 1991). This scenario is dubbed the deflagration-to-detonation transition (DDT; sometimes called delayed detonation).

★ E-mail: jason.sanders@ucl.ac.uk

It has further been hypothesized that in some systems the transition to detonation fails to occur so the WD undergoes a pure deflagration (e.g. Fink et al. 2014) leaving behind a remnant 'zombie' core. These systems could explain the observed class of underluminous Type Iax supernovae (Foley et al. 2013). Despite the success the single-degenerate DDT models have in explaining many properties of the observed light curve and remnant (e.g. Hoeflich & Khokhlov 1996; Badenes, Borkowski & Bravo 2005), a few issues remain:

(i) the stable accretion rate of hydrogen on to the WD surface must be within a relatively narrow range such that it can successfully reach the Chandrasekhar mass (if the rate is too high a red giant envelope can form leading to common envelope evolution unless a strong wind is driven; if too low hydrogen flashes and nova explosions eject the mass; Nomoto & Leung 2018);
(ii) there is an observed lack of near-Chandrasekhar mass WDs from which these systems could originate (e.g. Kepler et al. 2007);
(iii) the predicted rates from this channel fall short of explaining the observed SNe Ia rates (e.g. Ruiter, Belczynski & Fryer 2009 and see fig. 8 of Maoz et al. 2014 for a comparison);
(iv) low X-ray flux from nearby elliptical galaxies is consistent with only 5 per cent of all SNe Ia being single degenerate (Gilfanov & Bogdán 2010);
(v) the late-time spectrum of the Type Ia supernova (SN Ia) SN 2012cg lacks Hα emission as expected from the envelope of a non-degenerate companion (Shappee et al. 2018);
(vi) and there are still some inconsistencies in matching the colours, velocities, and light curves in all bands (Sim et al. 2013).

The double-degenerate scenario instead considers two WDs in a binary system (either both CO WDs, or a CO WD and a lower mass He WD) slowly merging due to the emission of gravitational waves (Iben & Tutukov 1984). Although early work presumed the disrupting WD would form an accretion disc around the primary (Benz et al. 1990) leading to steady growth up to $M_{\rm Ch}$, it is now deemed more probable that one WD initializes a detonation in the other well before the Chandrasekhar mass is reached. Lower central densities in the sub-$M_{\rm Ch}$ WDs lead naturally to production of intermediate-mass elements without invoking a deflagration phase. If He is accreted through Roche lobe overflow from a companion WD at a low enough rate to avoid helium flashes, a sufficiently massive He envelope can build up to initiate a detonation at the base of the He layer, triggering a detonation in the carbon core (Woosley & Weaver 1994). This scenario is called double detonation (double detonations may also occur in single-degenerate systems with a non-degenerate He-star, although these are expected to have short delay times so cannot explain the bulk of SNe Ia with >1 Gyr delays, and the initial detonation cannot be dynamically triggered, see below). The mass of the He shell required to initialize a detonation ($\sim$0.2 $M_\odot$) produces high-velocity iron-peak elements from the burning of the He shell not seen in observations (Hoeflich & Khokhlov 1996) and an overabundance of lighter iron-peak elements (e.g. V and Cr; Kobayashi, Leung & Nomoto 2020a). However, carbon detonation can occur with lower mass He shells (e.g. Fink et al. 2010) with the He detonation possibly being triggered dynamically through unstable mass transfer from a violent merger (Guillochon et al. 2010; Pakmor et al. 2012; Shen et al. 2018a). This scenario produces superior matches to observed multiband light curves (Kromer et al. 2010; Sim et al. 2010; Townsley et al. 2019) and also predicts the ejection of the WD companion at high velocities (see Shen et al. 2018b, for potential candidates from *Gaia*).

One route for constraining the contributions of these different SNe Ia formation scenarios is through galaxy chemical evolution modelling. SNe Ia produce $\sim$0.6 $M_\odot$ of iron (formed from the radioactive decay of ^{56}Ni which causes SNe Ia to glow) and low (although as discussed not insignificant) quantities of intermediate-mass α elements. The contribution of SNe Ia can then be inspected from the down-turning of a stellar population in the [α/Fe]–[Fe/H] diagram (Tinsley 1979). Although theoretical models for the different progenitor scenarios agree in the iron production per event, because of the variety of densities in the exploding media there is a range of different chemical abundances produced, particularly for the iron-peak elements. Most notably Mn (e.g. Seitenzahl et al. 2013b) and Ni (e.g. Kirby et al. 2019) are very sensitive to the central density of the exploding WD (see also McWilliam et al. 2018). Mn is mostly produced through the decay of ^{55}Co which is made in large quantities in normal freeze-out from nuclear statistical equilibrium achieved in $M_{\rm Ch}$ WDs, or in lower quantities in incomplete silicon burning at the lower densities typical in sub-$M_{\rm Ch}$ WDs, and is destroyed during α-rich freeze-out which occurs at lower densities (see Lach et al. 2020). Stable Ni is produced as ^{58}Ni which arises from the neutron-rich environments produced by electron capture in the high-density environments of $M_{\rm Ch}$ WDs (Seitenzahl & Townsley 2017). For these reasons, typically sub-$M_{\rm Ch}$ explosions lead to subsolar [Mn/Fe] and [Ni/Fe], whilst $M_{\rm Ch}$ events produce supersolar yields. Other elements (e.g. Cr, V) are also sensitive indicators of the explosion properties (Palla 2021). Studies of the [Mn/Fe] distribution in the Milky Way (MW) have thus concluded a significant fraction ($\gtrsim$75 per cent) of Chandrasekhar mass supernovae is required to explain the observations (Seitenzahl et al. 2013b; Kobayashi et al. 2020a), although comparative studies of different host environments [the bulge, thick disc, and dwarf spheroidal galaxies (dSphs); see Cescutti et al. 2008; North et al. 2012] have appealed to significantly metallicity-dependent SNe Ia yields. A significant fraction of sub-$M_{\rm Ch}$ systems are in line with the ejecta mass measurements from Scalzo, Ruiter & Sim (2014) who suggest 25–50 per cent of systems are inconsistent with $M_{\rm Ch}$ explosions, and Flörs et al. (2020) who suggest 85 per cent of spectroscopic Ni observations of SNe Ia are consistent with sub-$M_{\rm Ch}$ models. Recently, Kirby et al. (2019) and de los Reyes et al. (2020) have used Ni and Mn abundance measurements, respectively, for dSphs (most notably Sculptor) to argue subsolar [Mn/Fe] and [Ni/Fe] SNe Ia yields are needed, potentially indicating a high fraction of sub-Chandrasekhar mass events in these low-metallicity or early star-forming systems (Kobayashi et al. 2020a). Furthermore, McWilliam et al. (2018) have used the low [Mn/Fe] and [Ni/Fe] abundances of a single metal-rich star in Ursa Minor (UMi) to argue the star has been significantly enriched by a single sub-Chandrasekhar mass SNe Ia event. To build a consistent model of SNe Ia progenitors, we require a range of systems with different star formation histories and different metallicities that we can simultaneously fit.

With the arrival of data from the *Gaia* satellite (Gaia Collaboration et al. 2016), along with accompanying spectroscopic surveys, significant evidence has emerged that the MW experienced a $>10^{10}$ $M_\odot$ (total mass) merger approximately 8–10 Gyr ago. The progenitor system is known as the *Gaia* Sausage or *Gaia* Enceladus. Evans (2020) outlines the history of this idea. Nissen & Schuster (2010) discovered two populations of local halo dwarf stars with distinct kinematics that follow distinct chemical abundance tracks, and attributed the lower [α/Fe] sequence to a remnant dwarf galaxy. Deason et al. (2013) put forward the hypothesis that the prominent break in the Galactic stellar halo's density profile is the consequence of an ancient accretion of a substantial satellite galaxy. This idea was tested by Belokurov et al. (2018) who used early *Gaia* and Sloan Digital Sky Survey (SDSS) data to show that the bulk of the local MW's halo (corresponding to

intermediate metallicities [Fe/H] ~ -1.2 dex) is contributed by stars on very radial orbits. Comparing the *Gaia*–SDSS observations to cosmological simulations of MW-like galaxy formation, Belokurov et al. (2018) concluded that such a dominant, metal-rich, and highly eccentric halo component is naturally produced in a collision between the MW and a Large Magellanic Cloud(LMC)/Small Magellanic Cloud (SMC)-mass galaxy around redshift $z \sim 2$. Helmi et al. (2018) and Mackereth et al. (2019) presented a coherent chemo-dynamical picture of the merger using the Apache Point Observatory Galactic Evolution Experiment (APOGEE) data in combination with *Gaia* Data Release 2 (DR2), demonstrating that the progenitor's chemical evolution history can be reconstructed robustly using a set of simple orbital selection criteria. Further evidence for the merger has come from the properties of the globular cluster population (e.g. Myeong et al. 2018). The *Gaia* Sausage merger presents an ideal opportunity to study chemical evolution in a low-metallicity, 'high-redshift' galaxy using a sample of bright, nearby stars. Although the galaxy is no longer intact, we can still study the distributions of its constituent stars in chemical abundance space and make inferences on the evolution within the progenitor system (e.g. Vincenzo et al. 2019; Aguado et al. 2021; Matsuno et al. 2021). The system nicely bridges the gap between the lower metallicity dSph systems studied by Kirby et al. (2019) and de los Reyes et al. (2020) and the higher metallicity environments within the MW populations, whilst having abundant high-quality data. Furthermore, it is perhaps the best nearby example of a reasonably high-mass galaxy with a truncated early burst of star formation so presents a unique opportunity to study chemical evolution in this setting. With the current influx of high-dimensional abundance data from large stellar spectroscopic surveys such as APOGEE (Ahumada et al. 2020) and GALactic Archaeology with HERMES (GALAH; Buder et al. 2021), it is now possible to perform the necessary detailed studies of the chemical properties of this structure.

In this paper, we use a high-dimensional chemical abundance space to constrain simple chemical evolution models of the *Gaia* Sausage and place constraints on the properties of SNe Ia in this system. We discuss the data used in Section 2. In Section 3, we describe the models from Weinberg, Andrews & Freudenburg (2017) used to fit the data. Focussing specifically on the measured Mn and Ni yields, we discuss our results compared to a range of theoretical yields from $M_{\rm Ch}$ and sub-$M_{\rm Ch}$ SNe Ia in Section 4, along with the impact of the assumption of local thermal equilibrium on our results. Finally, we compare the constraints on the SNe Ia channel with results from other systems (the MW and dSphs) highlighting the necessary metallicity dependence of the yields, before we present our conclusions in Section 5.

2 MULTIDIMENSIONAL CHEMICAL ABUNDANCE DATA

We employ three samples of data: the local metal-poor 'halo' sample from Nissen & Schuster (2010), GALAH Data Release 3 (DR3; Buder et al. 2021), and APOGEE Data Release 16 (DR16; Ahumada et al. 2020). We describe the properties of each of the data sets in turn and the cuts we have employed to produce samples of *Gaia* Sausage member stars.

The *Gaia* Sausage is composed of stars on highly radial orbits with low to intermediate metallicities ($-1.7 \lesssim$ [Fe/H] $\lesssim -0.7$; Belokurov et al. 2018) that follow a clear sequence in the Tinsley–Wallerstein ([α/Fe] versus [Fe/H]) diagram (Helmi et al. 2018; Mackereth et al. 2019). We therefore select *Gaia* Sausage stars using a combination of a kinematic cut, a metallicity cut, and an ([Fe/H], [Mg/Fe]) cut. Kinematic cuts for *Gaia* Sausage stars have been performed in velocity space, action space, and eccentricity space (see Feuillet et al. 2020; Lane, Bovy & Mackereth 2021, for discussions of the differences). Here we opt for an eccentricity, e, cut which is equivalent to selecting a cone in energy versus angular momentum. This has the advantage of being restrictive at low energies so removes the high-[α/Fe] disc and Splash populations (Belokurov et al. 2020), but is less restrictive at higher energies where other accretion events may contaminate. Mackereth et al. (2019) and Naidu et al. (2020) both show that the *Gaia* Sausage does not contribute much local material with $e < 0.7$, but Kim et al. (2021) argue selecting $e > 0.7$ produces contamination from other merger events so advocate a stricter $e > 0.9$ cut to produce purer samples (see also Myeong et al. 2019). Even with a kinematic cut, high-metallicity 'splashed' or *in situ* stars contaminate. We therefore also employ a maximum metallicity cut. Using a high-latitude halo sample, Naidu et al. (2020) suggest that stars with $e > 0.7$ (and not members of the Sagittarius (Sgr) debris, Aleph, or the chemically defined *in situ*/Splash halo) are *Gaia*-Sausage-Enceladus stars. This sample has a maximum metallicity around [Fe/H] ≈ -0.6 dex (partly driven by the *in situ* halo definition used), although they acknowledge there is likely contamination in the sample from other structures. Fig. 1 of Mackereth et al. (2019) shows the rough divide between the low-[α/Fe] sequences of the MW and the *Gaia* Sausage is ~ -0.7 dex. Also in their figure it is evident that there is an intermediate [α/Fe] population with high eccentricity. Without a metallicity cut we pick up this feature and contaminate our sample. Fig. 1 and associated discussion in Belokurov et al. (2020) also demonstrate that the *Gaia* Sausage stars are limited to [Fe/H] < -0.7 dex and the high-eccentricity stars with higher metallicities are mostly all Splash. With these considerations, we primarily select *Gaia* Sausage stars as having $e > 0.85$ and [Fe/H] < -0.7 dex with a further ([Fe/H], [Mg/Fe]) cut defined below. We now describe the more specific cuts applied to each sample.

2.1 Nissen & Schuster (2010, 2011)

First, we take the nearby (distance < 335 pc) sample of low-metallicity dwarf stars from Nissen & Schuster (2010, hereafter NS10) and Nissen & Schuster (2011). The stars were observed with either the Ultraviolet and Visual Echelle Spectrograph (UVES) on the Very Large Telescope (VLT; $R \sim 55\,000$) or the FIber-fed Echelle Spectrograph (FIES) on the Nordic Optical Telescope (NOT; $R \sim 40\,000$), and local thermal equilibrium (LTE) abundance measurements were obtained from equivalent widths for Fe, Na, Mg, Si, Ca, Ti, Cr, Mn, Cu, Zn, Ni, Y, and Ba. For these stars we further utilize the non-LTE (NLTE) Cu measurements from Yan et al. (2016). We cross-match to the *Gaia* Early Data Release 3 (EDR3; Gaia Collaboration et al. 2016, 2021) to obtain proper motions and distances (utilizing a simple parallax inversion with a 0.017 mas offset), and find orbital properties (eccentricity e, maximum Galactic height $z_{\rm max}$) using GALPY (Bovy 2015) using the McMillan (2017) potential. We separate the *Gaia* Sausage stars from the *in situ* population by cutting on eccentricity (*Gaia* Sausage stars have $e > 0.7$; Mackereth et al. 2019; Naidu et al. 2020, although the stricter cut of $e > 0.85$ advocated above does not change the subsequent results significantly so NS10 results are shown using $e > 0.7$) and in the ([Fe/H], [Mg/Fe]) space (*Gaia* Sausage stars have [Mg/Fe] < -0.35[Fe/H] $- 0.07$). This results in 38 *Gaia* Sausage stars. The highest metallicity of the sample is -0.75 dex making an additional maximum metallicity cut (as done for the GALAH and APOGEE samples) unnecessary. We adopt the statistical uncertainties Δ[X/Fe] provided by NS10 and Nissen & Schuster (2011) (estimated from repeat observations) of (Mg, Si, Ca, Cr, Mn, Ni,

Cu, Zn)= (0.03, 0.03, 0.02, 0.02, 0.025, 0.01, 0.035, 0.035) dex and Δ[Fe/H]= 0.04 dex.

2.2 GALAH DR3

Secondly, we utilize the DR3 of the GALAH survey (Kos et al. 2017; Buder et al. 2021). GALAH is a large stellar spectroscopic survey performed with the HERMES spectrograph (Sheinis et al. 2015) on the Anglo-Australian Telescope. GALAH targets primarily stars with $9 < V < 14$, although the recent data release has processed similar surveys performed with HERMES, some of which are fainter. The majority of the targeted stars are within a few kpc of the Sun. In DR3, 30 elemental abundances are provided along with uncertainties, quality flags, and bitmasks indicating the lines used for each star. 11 of these elements have 1D NLTE corrections (Amarsi et al. 2020). Furthermore, GALAH DR3 provides several value-added catalogues including the computation of spectrophotometric distances incorporating *Gaia* DR2 data and orbital parameters (computed in the Galactic potential of McMillan 2017). We restrict to stars with $-2 <$ [Fe/H] < -0.7 dex (with `flag_sp` =0, `flag_fe_h` =0, and `flag_alpha_fe` =0) and select a sample of high-probability *Gaia* Sausage members by requiring med(e) > 0.85, $\Delta e < 0.05$, [Mg/Fe] < -0.2[Fe/H], and [Si/Fe] < 0.42 dex. The cut in the [Mg/Fe] versus [Fe/H] plane is different here compared to that adopted for NS10 and APOGEE DR16 due to the differences in the [Mg/Fe] abundance scales discussed in Appendix A. The [Si/Fe] cut removes obvious contaminants not observed in the other data sets. We remove stars within 3 half-light radii (in projection) of known globular clusters (Harris 1996, 2010 version) and within known open clusters (Dias et al. 2002). Furthermore, we only use the abundances with uncertainties smaller than 0.1 dex and with no flags. This results in a sample of 1047 stars.

In Appendix A, we inspect the abundance differences with respect to APOGEE DR16. We find significant offsets and trends with metallicity for many abundances. Part of this could arise from the NLTE corrections applied in GALAH. For Ni (which does not have a NLTE correction in GALAH), two lines are used in GALAH DR3. We find a significant difference in the residuals for stars analysed using both lines compared to when only one is used. We therefore choose to apply a correction to the GALAH DR3 Ni abundances to put them on the APOGEE scale.

2.3 APOGEE DR16

Thirdly, we use the APOGEE survey data as part of SDSS DR16 (Ahumada et al. 2020). APOGEE (Majewski et al. 2017) is a large infrared spectroscopic survey that has taken observations of ~430 000 stars in the H band at resolution $R \sim 22\,500$. The initial survey (APOGEE-1) used the 2.5-m Sloan Foundation Telescope (Gunn et al. 2006) situated at Apache Point Observatory, but from DR16 the survey was extended (APOGEE-2) to include additional data taken with the 2.5-m du Pont Telescope situated at Las Campanas Observatory. Both subsurveys used similar spectrographs (Wilson et al. 2019). Abundances for ~20 elements are provided as measured by the APOGEE Stellar Parameter and Chemical Abundances Pipeline (ASPCAP; García Pérez et al. 2016; Jönsson et al. 2018, 2020) along with uncertainties and quality flags. We only use data with `aspcapflag` =0 (and as with GALAH remove stars near known globular and open clusters). Unlike the GALAH survey, all abundances are derived under an LTE approximation, although NLTE corrections are expected in the next data release (Osorio et al. 2020). Leung & Bovy (2019) have provided a value-added catalogue with distances and orbital properties computed for all APOGEE stars via a convolutional neural network (ASTRONN). This catalogue assumes the MWPOTENTIAL2014 from Bovy (2015) whilst for the other data sets we have assumed the McMillan (2017) potential. For stars matching between APOGEE and GALAH with eccentricity uncertainties less than 0.1, the two catalogues give a median eccentricity difference of 0.01 with a scatter of 0.06 so the difference between the Galactic potentials is not a concern. We select stars with [Fe/H] < -0.7 dex, Δ[Fe/H] < 0.05 dex, Δ[Mg/Fe] < 0.05 dex, [Mg/Fe] < -0.35[Fe/H] $- 0.07$, $e > 0.85$, $\Delta e < 0.05$, and only use non-flagged abundances with uncertainties < 0.05 dex (0.1 dex for Cr and Cu). Abundances are not provided for low [X/H] which can lead to biases at low metallicities. This is most apparent for [Mn/H] which has a floor at -2.25 dex. This produces an upturn in the mean trend of [Mn/Fe] versus [Fe/H] below [Mn/Fe] ~ -1.5 dex. Our strict uncertainty cut removes [Mn/Fe] measurements below this value leading to unbiased results. The effect is weaker for the other abundances but again our cuts avoid any biases it might introduce. Our final sample consists of 819 stars.

2.4 Common stars

In Appendix A, we have analysed the differences in abundances for stars common to the three presented samples. When comparing APOGEE DR16 to NS10 we find only [Si/Fe] has a significant offset with APOGEE DR16 0.09 dex lower than NS10. The only significant offset between GALAH DR3 and NS10 is in [Cr/Fe] which is 0.11 dex lower in GALAH DR3 although there are only a few stars in common. When comparing APOGEE DR16 and GALAH DR3 the differences arising from the NLTE corrections of Mg, Si, and Ca from Amarsi et al. (2020) are apparent. Mn has NLTE corrections in GALAH but there is no significant systematic trend with respect to the APOGEE Mn abundances detected. As discussed in Section 2.2, the GALAH Ni abundances appear to be systematically biased at low metallicity compared to the APOGEE Ni abundances.

3 ANALYTIC CHEMICAL EVOLUTION MODELLING

Weinberg et al. (2017) demonstrate how galactic chemical evolution can be solved analytically under a number of simplifying assumptions:

(i) the galaxy is represented by a single 'zone' so no radial flows or radial migration are included;

(ii) the star formation efficiency (the star formation per unit gas mass $\equiv 1/\tau_\star$) is a constant (instead of scaling non-linearly as per a Kennicutt–Schmidt law);

(iii) supernovae (or other enrichment sources) either return their products immediately (e.g. for Type II) or, for Type Ia, according to an exponential delay-time distribution (DTD), $e^{-(t-t_D)/\tau_{Ia}}$, with time-scale τ_{Ia} and minimum delay time t_D (or a linear combination of such distributions);

(iv) stellar yields are independent of initial metallicity;

(v) the rate of gas outflow is proportional to the star formation rate, via a constant η;

(vi) the star formation history, $\dot{M}_\star(t)$, is from a limited set of functions including exponential $\dot{M}_\star \propto e^{-t/\tau_{sfh}}$ or linear–exponential $\dot{M}_\star \propto t e^{-t/\tau_{sfh}}$ for constant τ_{sfh}.

In these models, the gas reservoir is depleted on a time-scale $\tau_{dep} = \tau_\star/(1 - r + \eta)$, where $r \approx 0.4$ is the fraction of unprocessed material returned by stars (Weinberg et al. 2017). The advantage of these

models is the speed with which they can be evaluated as they avoid a costly forward integration.

For an assumed set of [initial mass function (IMF)-integrated] net yields $m_j^{\rm Y}$ of element j (i.e. mass of element produced per mass of stellar generation formed) and assuming a linear–exponential star formation law, the solution over time for the enrichment due to Type II supernovae (Y = II) is given by equation (56) of Weinberg et al. (2017), whilst the enrichment due to SNe Ia (Y = Ia) is given by equation (58). By normalizing these equations relative to an assumed solar abundance (Asplund et al. 2009), we are able to predict the abundance tracks [X/H](t) given a set of model parameters, $p = (\tau_{\rm sfh}, \tau_\star, \eta, \tau_{\rm Ia}, t_{\rm D})$. Furthermore, we define the yield abundance ratio for channel Y as $[{\rm X/Fe}]_{\rm Y} = \log_{10}(m_{\rm X}^{\rm Y}/Z_{{\rm X},\odot}) - \log_{10}(m_{\rm Fe}^{\rm Y}/Z_{{\rm Fe},\odot})$, where $Z_{j,\odot}$ is the solar mass fraction of element j.

The observed DTD for SNe Ia follows a power law of the form $\sim t^{-1}$ above some minimum delay time, $t_{\rm D}$ (Maoz & Mannucci 2012). As described in Weinberg et al. (2017), a linear combination of exponential DTDs, $\sum_{k=1}^{N_{\rm e}} w_k\, {\rm e}^{-(t-t_{\rm D})/\tau_{{\rm Ia},k}}$, can be used to approximate a power-law distribution over the times of interest. For each choice of $t_{\rm D}$ we have fitted a combination of $N_{\rm e} = 3$ exponential DTDs to $1/t^{1.1}$ normalized between $t_{\rm D}$ and a Hubble time. We have then approximated the relationship between $t_{\rm D}$ and the fitted time-scales, $\tau_{{\rm Ia},k}$, and relative weights, w_k, using cubic polynomials in the logarithms of these quantities. In this way, given a choice of $t_{\rm D}$ we can simply find the combination of exponential DTDs that reproduces the $1/t^{1.1}$ DTD. Our parameter set p is then reduced to $p = (\tau_{\rm sfh}, \tau_\star, \eta, t_{\rm D})$.

The key parameters for controlling the shape of the [X/Fe] versus [Fe/H] tracks are $\tau_{\rm sfh}$, $\tau_\star$, and $\tau_{\rm dep}$. Increasing $\tau_{\rm sfh}$ (slower enrichment), increasing $\tau_\star$ (less enrichment per unit gas mass), or decreasing $\tau_{\rm dep}$ (increasing η, more outflow) all cause the tracks in [α/Fe] versus [Fe/H] to turn over at lower [Fe/H]. In the instantaneous recycling approximation, a metallicity-dependent Type II yield is equivalent to changing the depletion time-scale, $\tau_{\rm dep}$, (higher yields at higher metallicity increase the effective depletion time-scale). Metallicity-dependent Type Ia yields are not possible within the analytic framework but would have a similar effect. Over the range of considered metallicities, theoretical yields depend only very weakly on metallicity (see later discussion).

We express this model in PYSTAN, a PYTHON interface to the probabilistic programming language STAN (Carpenter et al. 2017) for performing Bayesian inference. For each star i, we employ a birth time hyperparameter $t_i < t_{\rm max}$ from which we compute $\{[{\rm X/Fe}](t_i)\}$ and [Fe/H](t_i) to compare with the data. Assuming selection effects are minimal, the t_i follow the star formation rate, $t_i \sim \dot{M}_\star$, up to the maximum time $t_{\rm max}$ (when the *Gaia* Sausage merged with the MW and star formation ceased, Belokurov et al. 2020; Bonaca et al. 2020, or more precisely in our analysis, the time when the interstellar gas metallicity reaches the maximum metallicity, [Fe/H] ~ -0.7 dex, of our defined samples). By imposing this requirement, the models will fit the metallicity distribution of the data. We marginalize over the model parameters $p = (\tau_{\rm sfh}, \tau_\star, \eta, t_{\rm D}, t_{\rm max})$ adopting normal distributions[1] $t_{\rm D} \sim \mathcal{N}(0.15, 0.05)$ (with a minimum at 0.04 Gyr corresponding to the lifetime of a 8 $\rm M_\odot$ star assuming all more massive stars form Type II supernovae), $\tau_\star \sim \mathcal{N}(1, 100)$, $\eta \sim \mathcal{N}(10, 50)$, $t_{\rm max} \sim \mathcal{N}(4, 1)$, and $\tau_{\rm sfh} \sim \mathcal{N}(2, 1)$ (where all time-scales are in Gyr). We place broad priors on $[{\rm X/Fe}]_{\rm Y} \sim \mathcal{N}(0, 2)$ except for $[{\rm Mg/Fe}]_{\rm Ia}$ which should be small (e.g. Kobayashi, Karakas & Lugaro 2020b) so we adopt a prior $[{\rm Mg/Fe}]_{\rm Ia} \sim \mathcal{N}(-2, 0.4)$ with a hard upper limit of $[{\rm Mg/Fe}]_{\rm Ia} = -0.5$ (which approximately corresponds to the range of theoretical Type Ia models considered later). Early models (particularly those fitted to the GALAH data) produced $[{\rm Mg/Fe}]_{\rm Ia} \approx 0$ which is inconsistent with basic understanding of chemical evolution and essentially all SNe Ia models. For the mass of iron produced from Type II supernovae per total mass of stars formed, we use $\ln m_{\rm Fe}^{\rm II} \sim \mathcal{N}(\ln 0.00075, 0.45)$, which is consistent with a range of net IMF-integrated yields (evaluated at $10^{-1.5}\,{\rm Z_\odot}$) from the models of Chieffi & Limongi (2004), Kobayashi et al. (2006), Limongi & Chieffi (2018), and NuGrid (Pignatari et al. 2016; Ritter et al. 2018) using IMFs from Salpeter (1955), Kroupa (2001), Kroupa, Tout & Gilmore (1993), and Chabrier (2003) for stars between 0.1 and 100 $\rm M_\odot$. Similarly, for the range of Type Ia theoretical models considered later we find the mass of iron produced per event is $(0.77 \pm 0.15)\,{\rm M_\odot}$. The total number of SNe Ia over a Hubble time per stellar mass of star formation is approximately $(2.2 \pm 0.3) \times 10^{-3}\,{\rm M_\odot^{-1}}$ (Maoz & Mannucci 2012). Combining these numbers gives $\ln m_{\rm Fe}^{\rm Ia} \sim \mathcal{N}(\ln 0.0017, 0.24)$. In addition to the reported abundance uncertainties, we also allow for additional scatter in all [X/Fe] using a two-component mixture model with mixture weight $f_{\rm mix} \sim \mathcal{N}(1, 0.05)$ (where $f_{\rm mix}$ is the weight of narrower component restricted to $0 < f_{\rm mix} < 1$) and priors $\ln \boldsymbol{\sigma}_1 \sim \mathcal{N}(-3, 1)$and $\ln \boldsymbol{\sigma}_2 \sim \mathcal{N}(-1, 1)$ for the additive additional scatters. We also use the mixture for [Fe/H] but set $\sigma_1 = 0$.

[1] Adopting the notation $\mathcal{N}(\mu, \sigma)$ for a normal distribution with mean μ and variance σ^2.

3.1 Results

Figs 1–3 show the results of fitting these models to the NS10, GALAH DR3, and APOGEE DR16 *Gaia* Sausage samples, respectively. In Table 1, we give the model parameters governing the star formation, outflow, and DTD of the SNe Ia, and in Table 2, we give the abundances of the Type II and Type Ia channels. Here we discuss the results in general terms, mainly focusing on differences between the results from the different data sets. The next section concerns the meaning of the results in the context of nucleosynthesis in SNe Ia explosions.

In the NS10 data, we see little evidence for a plateau or knee in the [α/Fe] abundances for the *Gaia* Sausage stars suggesting the SNe Ia began contributing below [Fe/H] $= -1.5$ dex. This is somewhat corroborated by the APOGEE DR16 data where the knee occurs around [Fe/H] ≈ -1.5 dex. However, the picture is less clear from the GALAH DR3 data where there is seemingly a plateau until a metallicity of [Fe/H] ≈ -1 dex and the subsequent turnover due to the SNe Ia is less clear. All the studied α elements from GALAH DR3 have 1D NLTE corrections which may explain the differing behaviours. We can see in Table 1 that all models have a large $\tau_\star$ indicating inefficient star formation (high gas fraction) and high η indicating a large outflow. These features are necessary to explain the down-turning [α/Fe] at low metallicity. In Fig. 4, we show the star formation histories and iron enrichment over time are very similar despite the differences in parameters. The NS10 data are equally well fitted using the exponential star formation history which matches better the constraints from the GALAH DR3 and APOGEE DR16 data. Therefore, we conclude that the model parameter differences in Table 1 lead to moderate changes in the shapes of the tracks. More important is the variation in the abundances ($m^{\rm Y}$) which alters the slope of the tracks.

From Table 2 we see that all models produce $\sim$0.0015 $\rm M_\odot$ per solar mass of star formation, consistent with the prior of 0.0017 $\rm M_\odot$. On the other hand, the results for the iron contribution of Type II are slightly more varied with, in general, a larger contribution of

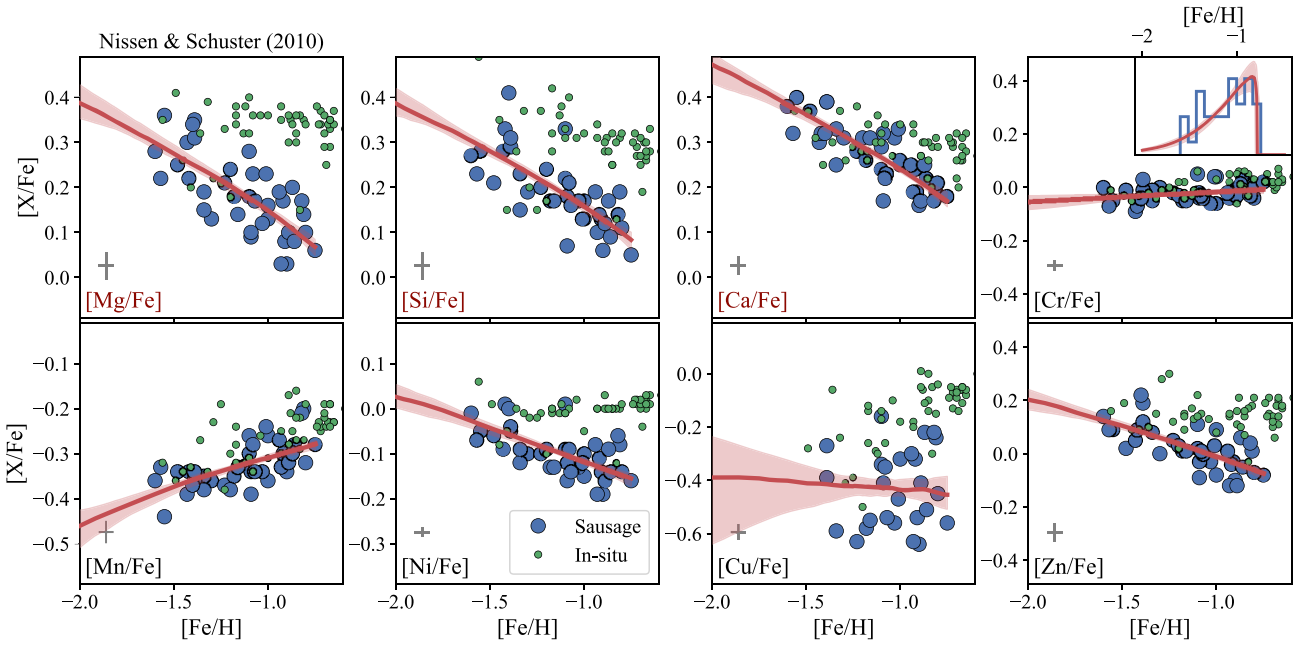

Figure 1. Analytic chemical evolution model fits to the Nissen & Schuster (2010) data set. Large blue points are stars kinematically and chemically selected to belong to the *Gaia* Sausage, whilst small green points are presumed *in situ* MW members. The red line and band show the fitted analytic chemical evolution models of Weinberg et al. (2017) with the uncertainty. The inset error bar shows the typical uncertainty in the abundances. The *y*-axis range spans 0.6 dex for all elements bar Cr, Cu, and Zn where a range of 1 dex is used. The top right-hand inset shows the 1D metallicity distribution and the model density. Note how even whilst [Mg/Fe] is declining with [Fe/H], [Mn/Fe] stays relatively flat indicating the low [Mn/Fe] contribution from the SN Ia channel.

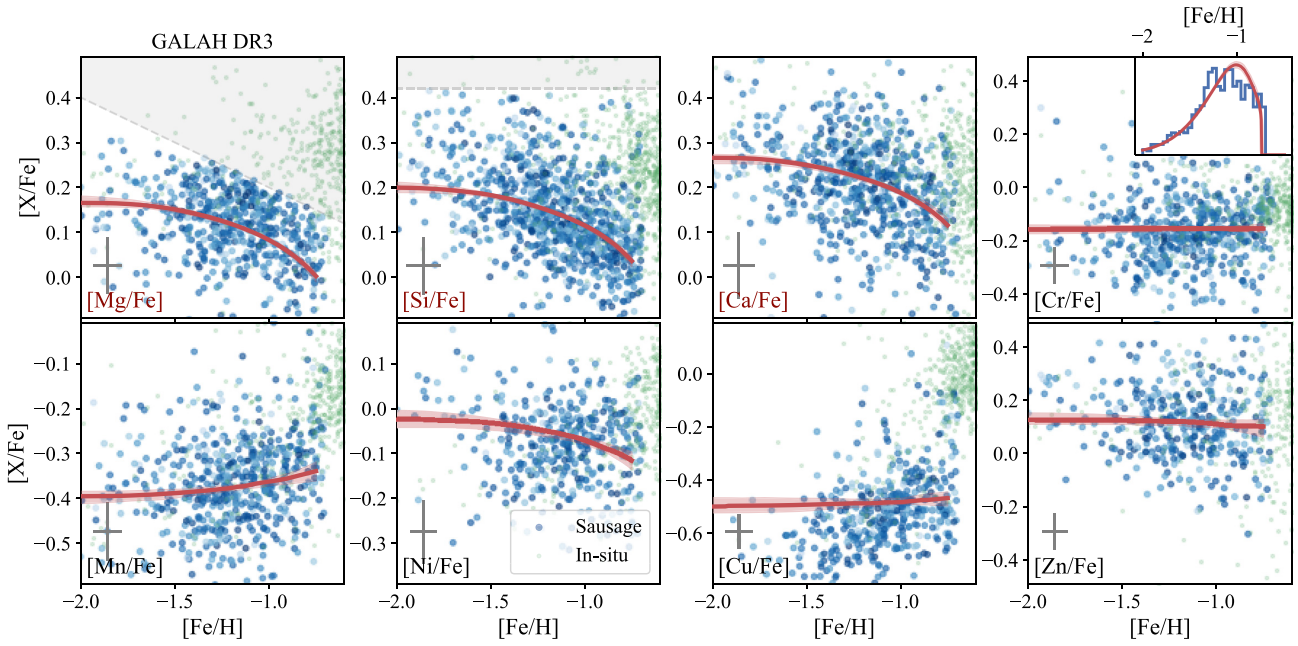

Figure 2. Analytic chemical evolution model fits to the GALAH DR3 data set (α element labels coloured red). Blue points are stars kinematically and chemically selected to belong to the *Gaia* Sausage with darker colours corresponding to stars on more eccentric orbits, whilst small green points are presumed *in situ* MW members. The red line and band show the fitted analytic chemical evolution models of Weinberg et al. (2017) with the uncertainty. The inset error bar shows the typical uncertainty in the abundances. The top right-hand inset shows the 1D metallicity distribution and the model density. 1D NLTE corrections are applied to Mg, Si, Ca, and Mn (Amarsi et al. 2020).

$\sim$0.0025 $M_\odot$ per solar mass of star formation compared to the prior of around $\sim$0.00075 $M_\odot$. This is driven by the shape of the metallicity distributions which may be subject to some selection effects, and is also sensitive to the specific choice of star formation history. However, it could also point towards the IMF of the *Gaia* Sausage producing more supernovae per generation. The α production of the Type II supernovae corresponds to the observed plateaus in each data set, and the differences between different data sets can largely

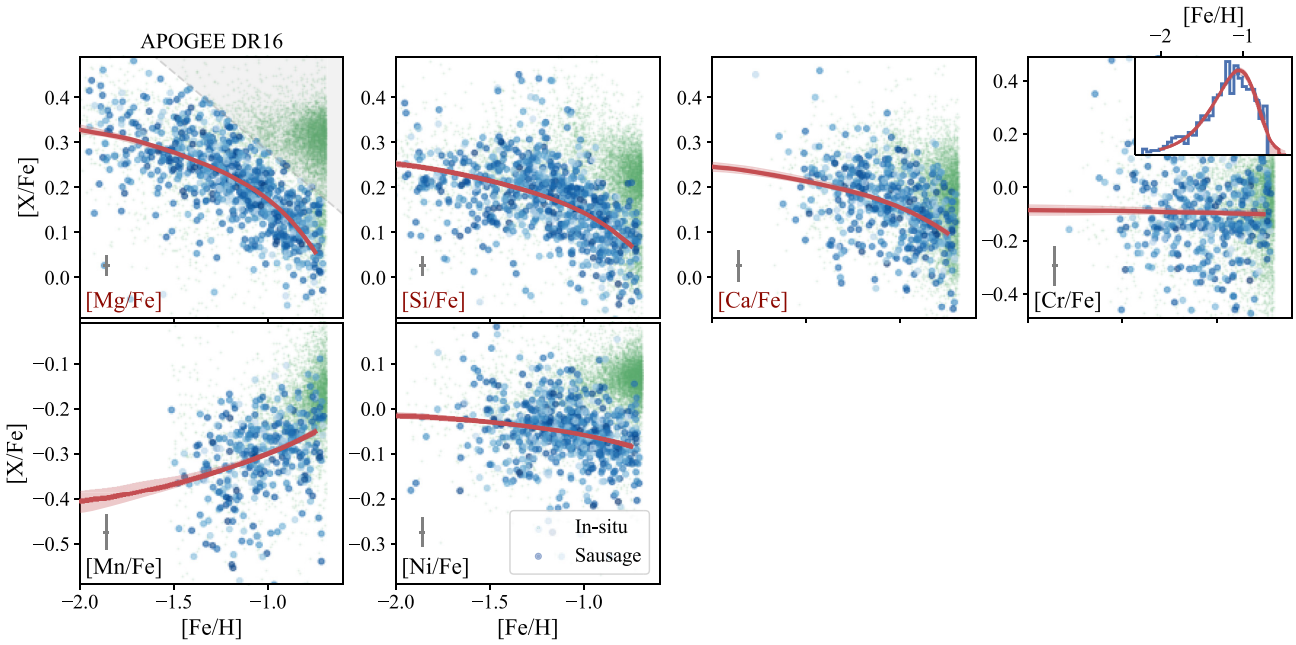

Figure 3. Analytic chemical evolution model fits to the APOGEE DR16 data set (α element labels coloured red). See caption of Fig. 2 for other details.

Table 1. Constraints and priors for parameters of the analytic chemical evolution models. All time-scales are in Gyr.

Parameter	Prior	NS10	GALAH DR3	APOGEE DR16
$\tau_{\rm sfh}$	2 ± 1	$2.4^{+0.7}_{-0.6}$	$1.0^{+0.2}_{-0.2}$	$0.9^{+0.3}_{-0.2}$
$t_{\rm max}$	4 ± 1	$4.4^{+0.9}_{-0.9}$	$3.9^{+1.0}_{-1.0}$	$5.1^{+0.8}_{-1.0}$
$\tau_\star$	1 ± 100	$17.6^{+7.0}_{-5.5}$	$21.8^{+8.9}_{-6.8}$	$15.4^{+5.5}_{-4.0}$
η	10 ± 50	$9.8^{+4.9}_{-3.9}$	$31.7^{+9.1}_{-6.9}$	$28.0^{+7.3}_{-5.8}$
$\tau_{\rm dep}$	–	$1.7^{+1.1}_{-0.6}$	$0.7^{+0.2}_{-0.2}$	$0.5^{+0.2}_{-0.1}$
$t_{\rm D}$	0.15 ± 0.05	$0.13^{+0.05}_{-0.05}$	$0.18^{+0.05}_{-0.05}$	$0.08^{+0.09}_{-0.03}$
$f_{\rm mix}$	1.00 ± 0.05	$1.00^{+0.00}_{-0.01}$	$0.86^{+0.02}_{-0.02}$	$0.90^{+0.01}_{-0.02}$

Table 2. Abundance constraints from analytic chemical evolution model fits. We report the (net IMF-integrated) mass per solar mass of star formation for Fe and the abundance relative to Fe for other elements. Type Ia yields are given in the top half of the table and Type II in the bottom half.

Type	Element	NS10	GALAH DR3	APOGEE DR16
Ia	$\log_{10} m_{\rm Fe}$	$-2.73^{+0.10}_{-0.10}$	$-2.89^{+0.09}_{-0.09}$	$-2.85^{+0.09}_{-0.09}$
Ia	[Mg/Fe]	$-2.00^{+0.35}_{-0.34}$	$-1.92^{+0.39}_{-0.37}$	$-1.96^{+0.36}_{-0.36}$
Ia	[Si/Fe]	$-0.87^{+0.34}_{-0.54}$	$-1.44^{+0.38}_{-0.51}$	$-0.31^{+0.05}_{-0.06}$
Ia	[Ca/Fe]	$-0.72^{+0.31}_{-0.52}$	$-0.78^{+0.33}_{-0.55}$	$-0.17^{+0.05}_{-0.05}$
Ia	[Cr/Fe]	$+0.03^{+0.03}_{-0.03}$	$-0.16^{+0.07}_{-0.09}$	$-0.12^{+0.05}_{-0.06}$
Ia	[Mn/Fe]	$-0.16^{+0.03}_{-0.03}$	$-0.24^{+0.05}_{-0.06}$	$-0.12^{+0.02}_{-0.02}$
Ia	[Ni/Fe]	$-0.41^{+0.08}_{-0.12}$	$-0.37^{+0.16}_{-0.26}$	$-0.17^{+0.02}_{-0.02}$
Ia	[Cu/Fe]	$-0.46^{+0.19}_{-0.35}$	$-0.42^{+0.10}_{-0.14}$	–
Ia	[Zn/Fe]	$-0.91^{+0.31}_{-0.52}$	$-0.01^{+0.15}_{-0.24}$	–
II	$\log_{10} m_{\rm Fe}$	$-3.08^{+0.16}_{-0.16}$	$-2.53^{+0.10}_{-0.10}$	$-2.71^{+0.10}_{-0.09}$
II	[Mg/Fe]	$+0.48^{+0.11}_{-0.09}$	$+0.17^{+0.01}_{-0.01}$	$+0.34^{+0.02}_{-0.02}$
II	[Si/Fe]	$+0.46^{+0.10}_{-0.09}$	$+0.20^{+0.01}_{-0.01}$	$+0.26^{+0.01}_{-0.01}$
II	[Ca/Fe]	$+0.54^{+0.10}_{-0.08}$	$+0.27^{+0.01}_{-0.01}$	$+0.25^{+0.02}_{-0.01}$
II	[Cr/Fe]	$-0.07^{+0.04}_{-0.06}$	$-0.15^{+0.02}_{-0.02}$	$-0.08^{+0.03}_{-0.03}$
II	[Mn/Fe]	$-0.56^{+0.11}_{-0.27}$	$-0.40^{+0.01}_{-0.01}$	$-0.42^{+0.03}_{-0.03}$
II	[Ni/Fe]	$+0.08^{+0.08}_{-0.06}$	$-0.03^{+0.02}_{-0.02}$	$-0.01^{+0.01}_{-0.01}$
II	[Cu/Fe]	$-0.41^{+0.19}_{-0.35}$	$-0.50^{+0.03}_{-0.03}$	–
II	[Zn/Fe]	$+0.29^{+0.10}_{-0.08}$	$+0.13^{+0.02}_{-0.02}$	–

be attributed to the observed discrepancies between common stars (due in part to NLTE effects). The Type Ia production of α elements is low for all data sets and elements. Mg is consistent with the prior, demonstrating our models are sufficiently flexible to reproduce the Mg trends without invoking significant Mg production. For all data sets we see Ca production is greater than Si production (relative to solar) but the different data set constraints are not consistent within the errors. This demonstrates the challenge of measuring the significant depletion of these elemental ratios.

We now focus on the iron-peak elemental abundances produced by the two channels. For all three data sets the three iron peak elements [Cr/Fe], [Mn/Fe], and [Ni/Fe] are all relatively flat with metallicity over the range where [α/Fe] is being depleted. In the case of Cr, this constrains the Type Ia and Type II abundance ratios to be very similar. The Type Ia yield for GALAH DR3 and APOGEE DR16 are similar and slightly subsolar, whilst NS10 is essentially solar, consistent with the discrepancies in the abundances for common stars discussed in Section 2.4. For Mn there is a weak positive slope present in all three data sets but most clearly in NS10. This indicates a low (subsolar) Type Ia Mn enrichment of around [Mn/Fe] ~ -0.15 dex. [Ni/Fe] has a negative slope with metallicity in all data sets (note that using the uncorrected GALAH DR3 Ni abundances we found a positive slope). As with [Mn/Fe], this points to a subsolar [Ni/Fe] contribution from Type Ia. For both Mn and Ni, the measurements from all three data sets are consistent within the errors.

Cu and Zn are also produced predominantly in supernovae but with very weak contributions from the asymptotic giant branch (AGB) stars (e.g. Kobayashi et al. 2020b). Additionally, as an odd-Z element, Cu production (particularly from Type II supernovae)

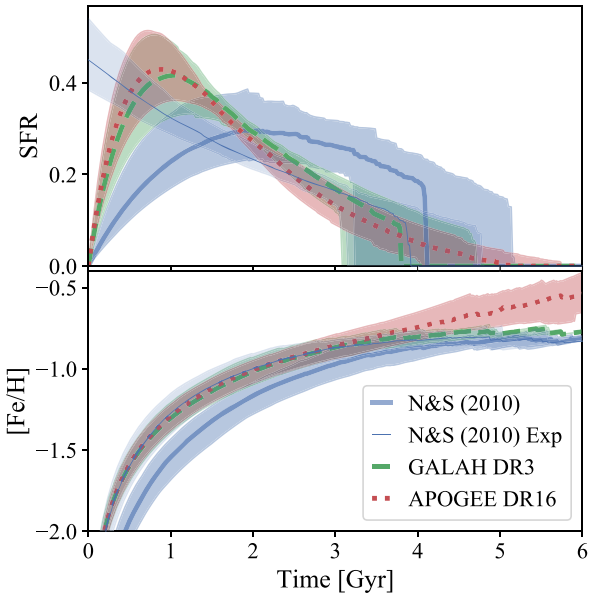

Figure 4. Comparison of the star formation history (top) and iron abundance over time (bottom) for the three *Gaia* Sausage data sets: Nissen & Schuster (2010, N&S) in blue solid (with the exponential model variant shown with a thinner line), GALAH DR3 (Buder et al. 2021) in green dashed, and APOGEE DR16 (Ahumada et al. 2020) in red dotted.

appears sensitive to metallicity (Kobayashi et al. 2020b). The model fits do not completely capture the trends in the GALAH data, possibly for this reason, although for Zn in particular the scatter is large. Despite these caveats, our results indicate a typical [Cu/Fe] from Type Ia of ~ -0.5 dex. The downwards trend in [Zn/Fe] from the NS10 data gives [Zn/Fe] ~ -1 dex, whilst the GALAH DR3 produces a result around solar (although the results are marginally consistent within the errors).

As a check of the robustness of the results, we also considered the exponential star formation law solution from Weinberg et al. (2017) and found the model fits and the conclusions regarding the inferred yields very similar (see Table B1 for a comparison for the NS10 data set).

4 DISCUSSION

We now discuss the constraints derived from the chemical evolution models of the *Gaia* Sausage with comparison to theoretical calculations of SNe Ia yields and similar constraints for dSph data.

4.1 Theoretical models

As discussed in the Introduction, we consider three main categories of theoretical SNe Ia explosion calculation: DDT, pure deflagration, and double-detonation models. All considered models (bar one) follow a single WD system that is triggered to explode in a variety of ways. We evaluate the theoretical yields for a SN Ia with metallicity $Z = 10^{-1.2}$ $Z_\odot$ by linearly interpolating in $\log_{10}(Z)$ or if $Z = 10^{-1.2}$ $Z_\odot$ is not covered by the grids, we use the lowest available metallicity model. Only the pure deflagration WDD2 model of Leung & Nomoto (2018), the pure deflagration model of Fink et al. (2014), and the violent merger model of Pakmor et al. (2012) are only available at solar metallicity.

4.1.1 Deflagration-to-detonation transition models

Deflagration-to-detonation transition (DDT) models are the favoured types of models for $M_{\rm Ch}$ SNe Ia. A subsonic deflagration phase is introduced in a CO WD which initially burns at high density producing iron-group elements. This causes the star to expand producing lower density regions containing unburnt fuel. After $\sim$1 s the transition occurs to a supersonic detonation phase that burns the remaining fuel predominantly producing intermediate-mass elements (such as Si) due to the now lower densities. The deflagration flame front is highly textured in this scenario so multidimensional models are essential. We consider three different sets of models. Seitenzahl et al. (2013a) present yields from 3D DDT models using a varying number of ignition sites and four metallicities ($Z = 1$, 0.5, 0.1, and 0.01 $Z_\odot$). We use the benchmark models with 100 ignition sites and a central density of 2.9×10^9 g cm^{-3} which produce $\sim$0.6 $M_\odot$ of ^{56}Ni. The strength of the deflagration phase increases with the number of ignition sites, which decreases the production of Fe, Cu, and Zn but increases the production of intermediate-mass elements due to increased energy injection and expansion and increases the production of Cr, Mn, and Ni. Leung & Nomoto (2018, LN18) ran a series of 2D DDT models with a range of central densities, metallicities, C/O ratios, and ignition kernels. We consider their benchmark models with central density 3×10^9 g cm^{-3} at $Z = 0$, 0.1, 0.5, 1, 2, 3, 5 $Z_\odot$ which produce 0.63 $M_\odot$ of ^{56}Ni, and their updated WDD2 model (Iwamoto et al. 1999) which we denote LN18WDD2. Kobayashi et al. (2020a) updated the models of Leung & Nomoto (2018) using a more realistic solar-scaled initial composition (elements lighter than Ne are presumed to be converted into Ne during normal H and He burning), again varying both the initial mass and metallicity ($Z =$ 0–0.04). As in Leung & Nomoto (2018), the $M_{\rm Ch}$ model with a central density of 3×10^9 g cm^{-3} produced 0.63 $M_\odot$ of ^{56}Ni. Lower masses produce more Fe and less Si, Ca, Cr, Mn, Ni, and Zn. We consider all four mass models (1.30, 1.33, 1.37, 1.38 $M_\odot$). We denote the models as K20DDT_M$*$. The lower of these masses can be considered as sub-$M_{\rm Ch}$ models. However, the difference with the double-detonation scenario (see below) is that central carbon ignition does not initiate a detonation due to the high electron-degeneracy pressure, but rather a deflagration. Also, in these cases, the physical trigger for the explosion is not clear. Prior to ignition, a near-$M_{\rm Ch}$ WD undergoes a simmering period where low-level carbon burning slowly increases the neutron fraction. This is equivalent to imposing a floor on the metallicity of the WD of $Z/Z_\odot \approx 2/3$ (Piro & Bildsten 2008). The models of Kobayashi et al. (2020a) and Seitenzahl et al. (2013a) have relatively weak metallicity dependence on the Mn production so we ignore this detail.

4.1.2 Pure deflagration models

Pure deflagrations (Def) have been proposed as scenarios to explain Type Iax supernovae (spectroscopically similar to Type Ia but with lower peak brightness; Foley et al. 2013). The deflagration does not completely destroy the star and they primarily produce intermediate-mass elements with lower iron yields and an overabundance of neutron-rich species (e.g. ^{58}Ni). Their contribution to galactic chemical evolution is believed to be quite small (Kobayashi et al. 2020b). Fink et al. (2014) ran 3D pure deflagration models using a similar set-up to Seitenzahl et al. (2013a). We select the model with 100 detonation sites. Mn production has a weak dependence ($\sim$0.2 dex variation) on the number of ignition sites as shown in de los Reyes et al. (2020). We also take the 2D pure deflagration models from Leung & Nomoto (2018, LN18Def). Leung & Nomoto (2018)

have rerun the classic W7 model of Iwamoto et al. (1999) using updated electron capture rates and run a series of new models with varying central density. We take the model with a central density of 10^9 g cm^{-3} (LN18W7). Higher central densities lead to higher Mn yields.

4.1.3 Double-detonation models

Double-detonation models are the favoured scenario for sub-$M_{\rm Ch}$ SNe Ia. In this scenario, He is accreted on to the surface of the CO WD from a non-degenerate He-star, a companion He WD or even another CO WD as they are expected to have a small surface He layer. The He shell ignites and detonates at the base of the layer when it becomes sufficiently massive or if driven dynamically through the violent merger of two WDs (Pakmor et al. 2012). This initial detonation triggers a subsequent detonation in the C/O core. There are two general classes of these controlled detonation models: those with and without a He shell. The He shell is required to initiate the first detonation but as observations suggest only a low mass He shell is required (Kromer et al. 2010), several groups have run pure detonation simulations without a He shell (e.g. Sim et al. 2010). Both Shen et al. (2018a) and Bravo, Badenes & Martínez-Rodríguez (2019) ran 1D bare detonation simulations. Bravo et al. (2019) considered five WD masses at five metallicities at two ^{12}C + ^{16}O reaction rates (standard and reduced by a factor of 10). Here we use the 1.06 M$_\odot$ model with standard ^{12}C + ^{16}O reaction rate. Similarly, Shen et al. (2018a) ran 1D bare detonation models at different masses, metallicities, C/O compositions, and ^{12}C + ^{16}O reaction rates. We use the 1 M$_\odot$ model with C/O = 50:50 and standard ^{12}C + ^{16}O reaction rate. As discussed by Gronow et al. (2021a) for example, although of low mass, the He shell is important to the explosion mechanism and subsequent yields of the model. Leung & Nomoto (2020) ran a series of 2D double-detonation simulations varying the core mass, the He shell mass, metallicity, and initial He detonation mechanism. We consider their benchmark model with core mass $M = 1.1$ M$_\odot$, a 0.1 M$_\odot$ He shell, and detonated with a bubble 50 km above the core–envelope interface (110-100-x-50) that produces 0.62 M$_\odot$ of ^{56}Ni. We also consider the benchmark models with a spherical detonation which have $M = 1.0$ M$_\odot$ and a 0.05 M$_\odot$ He shell (100-050-x-S50). Differences in the detonation geometry are largely characterized by differences in the abundances of light iron-peak elements (e.g. V and Cr) with aspherical detonations producing higher abundances of these elements (Leung & Nomoto 2020; Palla 2021, although note that the two inspected models differ in their He shell mass which also affects these elements). As with the DDT models, the models of Leung & Nomoto (2020) were updated with a more realistic initial mix of heavy elements by Kobayashi et al. (2020a) who ran models at a series of core masses and metallicities ($Z = 0$–0.04) with 0.05 M$_\odot$ He shell and a spherical detonation pattern. We use the 1, 1.1, and 1.2 M$_\odot$ total mass models, ignoring the 0.9 M$_\odot$ model as it produces a low quantity of Fe. The 1 M$_\odot$ model produces 0.63 M$_\odot$ of ^{56}Ni. Very recently, Gronow et al. (2021a,b) have presented a series of 3D double-detonation models investigating a range of core masses and He shell masses, and post-processed for a range of metallicities ($Z = 0.01, 0.1, 1, 3$ Z$_\odot$). We use the models with 0.9 and 1 M$_\odot$ core mass and 0.05 M$_\odot$ He shell which produce around 0.6 M$_\odot$ of ^{56}Ni, and ignore the 0.8 M$_\odot$ model as the iron production is low. Despite similar core and shell masses, the Gronow et al. (2021a,b) model yields differ significantly from those of Kobayashi et al. (2020a) possibly related to the core-shell mixing in Gronow et al. (2021a,b), the difference in the dimensionality of the models, or the difference in the nuclear network size (seven isotopes in Kobayashi et al. 2020a compared to 35 in Gronow et al. 2021a,b) as for the low-density regions found in sub-$M_{\rm Ch}$ WDs some burning pathways are neglected by smaller networks (Shen et al. 2018a).

The described bare and double-detonation models all follow the explosion of a single WD presuming some initial configuration from the result of an ongoing merger event. Simulations of the violent mergers of two WDs (Pakmor et al. 2012) have been considered but there are more limited available nucleosynthetic yields for this case due to the increased complexity of the simulations. A set of four violent merger models from Pakmor et al. (2010, 2012) and Kromer et al. (2013, 2016) are available through the Heidelberg Supernova Model Archive (HESMA) data base.[2] Of these, only the model of Pakmor et al. (2012, P12_VM_11_09) of a 1.1 and 0.9 M$_\odot$ WD merger produces a reasonable quantity of Fe ($\sim$0.6 M$_\odot$) so we ignore the others. This model is essentially a pure/bare detonation model. As Seitenzahl et al. (2013b) report, the model produces [Mn/Fe] = -0.15 dex.

4.1.4 Comparison with observations

Fig. 5 shows the Type Ia abundance constraints from the *Gaia* Sausage data sets with the theoretical yields from the different models. We show the five iron-peak elements in our modelling (Cr, Mn, Ni, Cu, and Zn). Focusing on Mn and Ni, we see that all models lie along an anticorrelation in [Mn/Fe]$_{\rm Ia}$ versus [Ni/Fe]$_{\rm Ia}$ as highlighted by Kobayashi et al. (2020a). As discussed in the Introduction, these elements are particularly sensitive to the density and hence mass of the model. Pure deflagration models sit at the high-abundance end of the trend along with the DDT models. The lower mass DDT models of Kobayashi et al. (2020a) sit further down the trend with the sub-$M_{\rm Ch}$ models as they too can be considered as sub-$M_{\rm Ch}$ models. The violent merger model of Pakmor et al. (2012) sits part way between the two groups of models. It is clear our derived constraints are able to distinguish between the different scenarios. Based on this panel alone, all data sets are consistent with either

(i) the 1 M$_\odot$ Gronow et al. (2021a,b) model;
(ii) a mixture of 'normal' DDT (40 per cent) and sub-$M_{\rm Ch}$ (60 per cent) Kobayashi et al. (2020a) models (as shown in the plot);
(iii) the violent merger model of Pakmor et al. (2012); or
(iv) a low-mass 1.33 M$_\odot$ DDT model (which is perhaps not well physically motivated).

The distribution of the models in Cr abundances is not so easy to understand and is perhaps more reflective of the ignition mechanism rather than its structure (Palla 2021). There are DDT models and sub-$M_{\rm Ch}$ models consistent with the solar/subsolar measured abundances. The mixture model matches the NS10 well and as discussed these are systematically higher than the corresponding GALAH DR3 and APOGEE DR16 models. Finally, Cu and Zn are heavier iron-peak elements largely produced in the detonation phase (e.g. Kobayashi et al. 2020a). We observe that deflagration models are inconsistent with the constraints. Also, despite its success in reproducing [Mn/Fe] and [Ni/Fe], the violent merger model underproduces both of these elements. Sub-$M_{\rm Ch}$ models tend to produce more Cu than DDT models producing better consistency with the data. The Zn measurements of essentially all DDT and sub-$M_{\rm Ch}$ models are consistent with the data.

[2] https://hesma.h-its.org

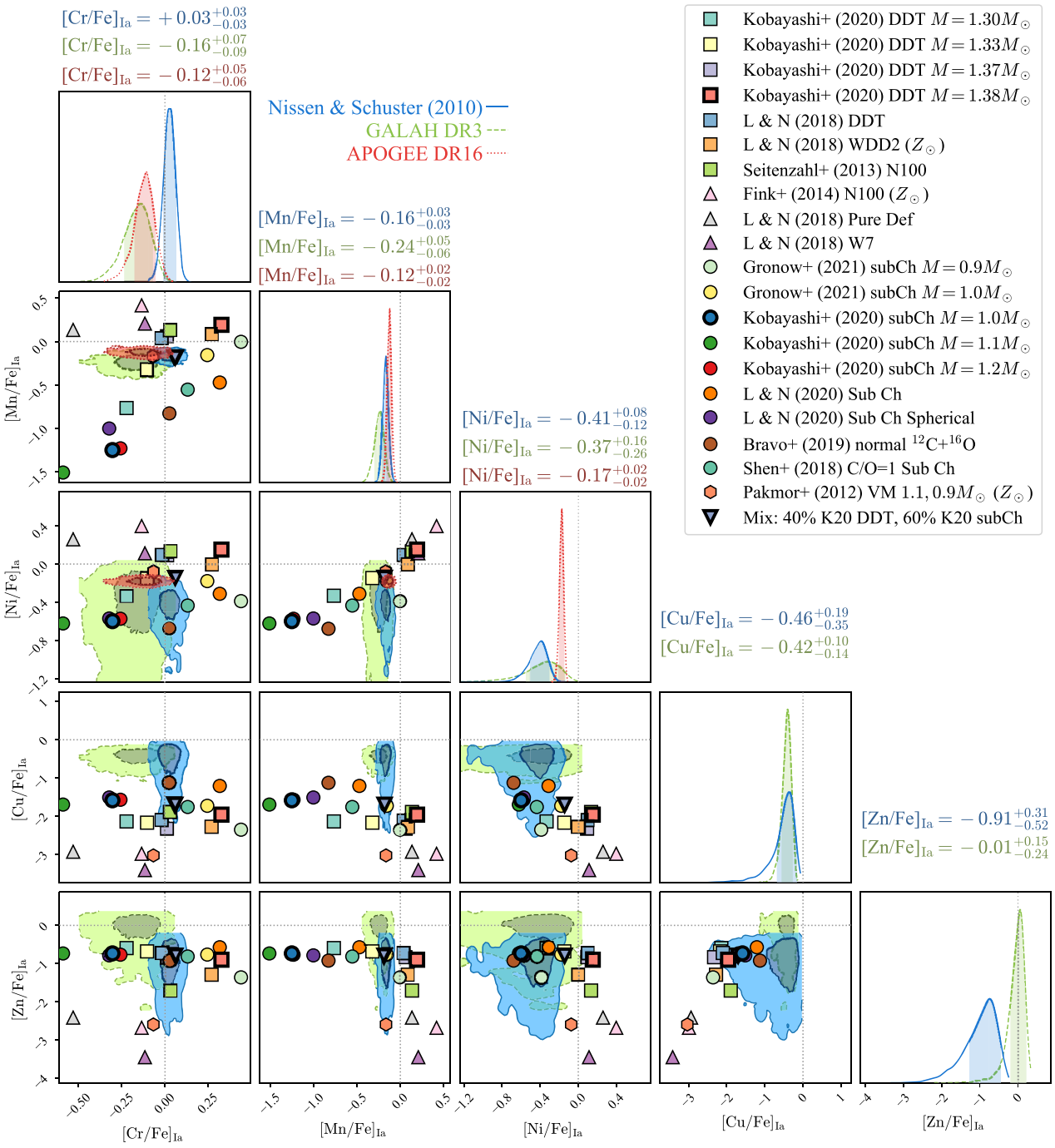

Figure 5. Constraints on the elemental yields from SNe Ia determined from the NS10 (blue solid), GALAH DR3 (green dashed), and APOGEE DR16 (red dotted) *Gaia* Sausage samples compared to theoretical yields from the literature. Squares denote deflagration-to-detonation transition (DDT) scenarios, triangles are pure deflagrations (Def), and circles are sub-Chandrasekhar mass double-detonation Type Ia models (see Section 4.1 for a detailed discussion of the different models). Although no model set exactly reproduces all of the data, note how the sub-Chandrasekhar mass models produce lower quantities of Mn and Ni consistent with the observations. Vertical and horizontal dashed lines are the solar values.

In Fig. 6, we show a larger version of the $[Mn/Fe]_{Ia}$ versus $[Ni/Fe]_{Ia}$ panel of Fig. 5 with only the two benchmark M_{Ch} and sub-M_{Ch} models of Kobayashi et al. (2020a) shown. We also display the sequence of linear combinations of these two models. The APOGEE DR16 constraints agree very well with a mixture of 60 per cent sub-M_{Ch} SNe Ia. Both the NS10 and GALAH DR3 are less conclusive in this 2D projection, although they are consistent at the 2σ level with the APOGEE result. The $[Mn/Fe]_{Ia}$ measurement is more robust as for GALAH DR3 [Ni/Fe] we adjusted it based on overlaps with APOGEE. Also $[Ni/Fe]_{Ia} < [Ni/Fe]_{II}$ whilst $[Mn/Fe]_{Ia} > [Mn/Fe]_{II}$ meaning we can be more confident about the Mn contribution from SNe Ia. In the inset panel of Fig. 6, we display the inferred sub-M_{Ch} percentage based on the Mn measurements alone. GALAH DR3 yields slightly higher percentages of ∼65 per cent, whilst NS10

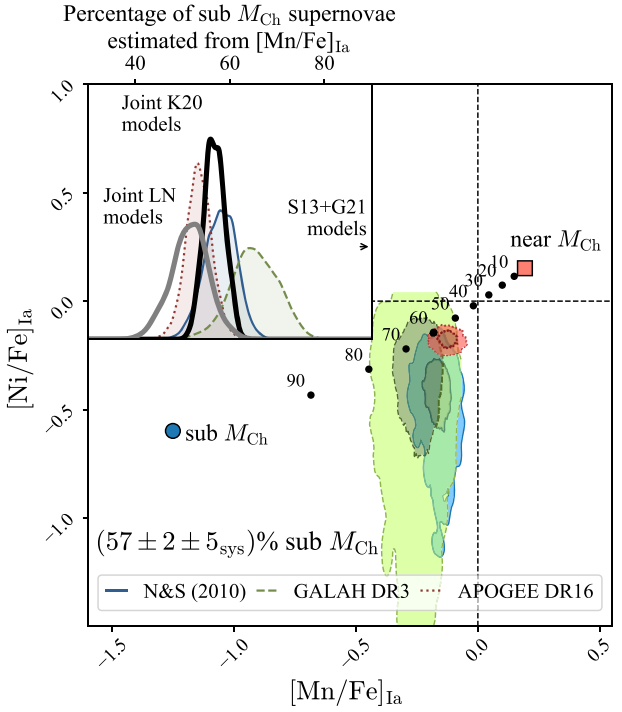

Figure 6. Constraints on the nickel and manganese yields from SNe Ia determined from NS10 (blue solid), Buder et al. (2021) (green dashed), and Ahumada et al. (2020) (red dotted) *Gaia* Sausage samples. A M_{Ch} deflagration-to-detonation transition (DDT) model and a sub-M_{Ch} double-detonation model are shown by the coloured points (both from Kobayashi et al. 2020a) and the sequence of black points show the different ratio combinations labelled by the percentage of sub-M_{Ch} supernovae. The inset shows the inferred percentage of sub-Chandrasekhar SNe Ia required to reproduce the Type Ia [Mn/Fe] measurements. The coloured figure shows the individual sample results assuming the models of Kobayashi et al. (2020a), whilst the black figure shows the combined result. The grey figure shows the combined result assuming the models of Leung & Nomoto (2018, 2020) which adopt a different initial composition. The arrow shows the 95 per cent lower bound using the models of Seitenzahl et al. (2013a) and Gronow et al. (2021a,b).

and APOGEE DR16 are more consistent with ∼55 per cent. This is despite there being minimal differences in the Mn abundances from common stars so the difference must be driven by how the distribution of all the abundances constrains the SNe Ia contribution. Combining the constraints gives (57 ± 2) per cent sub-M_{Ch}. Adopting instead the Kobayashi et al. (2020a) 1.1 or 1.2 $M_\odot$ total mass sub-M_{Ch} models yields essentially identical constraints of 56 and 57 per cent, respectively, so any mass distribution of sub-M_{Ch} WDs would produce a similar constraint.

If instead we adopt the models of Leung & Nomoto (2018) (which include only ^{22}Ne for the metallicity rather than a scaled-solar composition and so are perhaps less realistic), we yield ∼52 per cent sub-M_{Ch} using the 1.1 $M_\odot$ core mass sub-M_{Ch} model and ∼40 per cent using the spherical detonation 1.0 $M_\odot$ model. The more recent metallicity-dependent 3D sub-M_{Ch} models from Gronow et al. (2021a,b) in general produce significantly higher [Mn/Fe] than the Kobayashi et al. (2020a) models. The 1 $M_\odot$ core mass model implies essentially 100 per cent sub-M_{Ch} supernovae ($\gtrsim$87 per cent sub-M_{Ch} SNe Ia at 95 per cent confidence), whilst the 1.1 $M_\odot$ core mass model requires (67 ± 3)per cent sub-M_{Ch} (if combined with the Seitenzahl et al. 2013a models) and the 0.9 $M_\odot$ produces too high [Mn/Fe] to be consistent with the data. Although our inference is still quite uncertain as it depends on the specific models we adopt, the general conclusion of a significant fraction of sub-M_{Ch} appears robust.

4.2 Non-LTE effects

Mn abundance measurements are known to be sensitive to the assumption of local thermal equilibrium (LTE; Bergemann & Gehren 2008; Bergemann et al. 2019). As our conclusions regarding the SNe Ia enrichment channel depend on Mn, it is worth discussing the status of non-LTE (NLTE) corrections for Mn. In general, the difference between 1D NLTE Mn abundances and 1D LTE Mn abundances (Δ_{NLTE}) is positive, increases for lower metallicity stars and is typically larger for giant stars than dwarf stars, although the differences are line dependent with resonance lines more sensitive to NLTE effects. The metallicity dependence has the effect of steepening correlations in [Mn/Fe] versus [Fe/H] when using LTE abundances. Battistini & Bensby (2015) used the corrections from Bergemann & Gehren (2008) to produce NLTE Mn abundances for a sample of G dwarfs finding a very flat, near-solar [Mn/Fe] versus [Fe/H] distribution for $-1 \lesssim$ [Fe/H] $\lesssim 0.5$. However, the updated NLTE corrections from Bergemann et al. (2019) suggest a shallower trend of Δ_{NLTE} with metallicity. Eitner, Bergemann & Larsen (2019) use the updated model to compute (line-dependent) corrections for [Fe/H] = −2 dex models finding $\Delta_{NLTE} = 0.2$–0.25 dex for dwarf stars and $\Delta_{NLTE} = 0.35$–0.4 dex for giants. Eitner et al. (2020) applied the new corrections to dwarf and giant stars in the range $-3 \lesssim$ [Fe/H] $\lesssim 0$ finding a slowly rising [Mn/Fe] with [Fe/H] from [Mn/Fe] ≈ −0.2 dex at [Fe/H] ≈ −2 dex to [Mn/Fe] ≈ 0 dex at [Fe/H] ≈ 0 dex. Five stars in the Eitner et al. (2020) sample are in the NS10 sample. Ignoring the measurement for HD 121004 which is based upon a Mn II line, we find the difference between the Eitner et al. (2020) NLTE measurements and the Nissen & Schuster (2011) LTE measurements is ∼0.07 dex but they do not show a significant increase with decreasing metallicity.

The Nissen & Schuster (2011) Mn measurements are based upon Mn I lines at 4783.4, 4823.5, 6013.5, 6016.7, and 6021.8 Å. The lines around 6015 Å are weaker and not detectable at low (∼−1.4 dex) metallicity. However, the lines around 4800 Å are strong but ignored in cool, metal-rich stars (they can also lie outside the UVES spectral range). Assuming the dwarf model from Bergemann et al. (2019) both of these sets of lines have $\Delta_{NLTE} = 0.04 - 0.105$[Fe/H]. This can be compared to the correction in fig. 12 of Amarsi et al. (2020) which gives $\Delta_{NLTE} \approx -0.1$[Fe/H] (independent of whether the star is a dwarf or giant, although Bergemann et al. 2019 suggest larger corrections for giants: $\Delta_{NLTE} \approx 0.2 - 0.1$[Fe/H], but they do not provide results for the GALAH lines 4754.04 and 4761.51 Å). We have applied the Bergemann et al. (2019) dwarf NLTE correction to the NS10 data and refitted the chemical evolution models, despite the direct comparison of the four stars in Eitner et al. (2019) suggesting this correction is too large. This fit produces $[Mn/Fe]_{Ia} = (-0.17 \pm 0.04)$ dex, near identical to the results using the 1D LTE. The bigger difference is in the Type II yields which are ∼0.2 dex higher at $[Mn/Fe]_{II} = (-0.18 \pm 0.05)$ dex. This higher Mn production could be matched by the yields of Chieffi & Limongi (2004) or the fast rotating models of Limongi & Chieffi (2018). The GALAH DR3 abundances already include the 1D NLTE corrections for Mn yet yield a higher $[Mn/Fe]_{Ia}$ than the corrected NS10 data. It should also be noted that similar trends in [Mn/Fe] versus [Fe/H] for the NS10 data set are seen in both the *Gaia* Sausage and the higher α *in situ* or Splash (Belokurov et al. 2020) stars. As noted in Nissen & Schuster (2011), this does suggest some part of the trend is due to

NLTE effects although clearly the two groups are still distinct in this projection.

The 1D NLTE corrections do not tell the full story, as 3D corrections are also important for Mn. However, 3D calculations are expensive so much more limited information is available. Bergemann et al. (2019) compute the difference between 1D and 3D NLTE calculations for a set of four models (giant and dwarf at [Fe/H] $= -1, -2$ dex) finding, in general, 3D NLTE Mn abundances are larger than 1D NLTE. From Bergemann et al. (2019) the lines around 4800 and 6015 Å in dwarf stars have 3D NLTE larger than 1D by 0.06 and 0.08 dex, respectively. Applying this correction to our data set will shift the measurement of $[Mn/Fe]_{Ia}$ up by ∼0.05 dex which would lower the contribution of sub-M_{Ch} to around 50 per cent in line with the MW result from Seitenzahl et al. (2013b).

GALAH uses the lines at 4754.04 and 4761.51 Å which have 3D NLTE larger than 1D NLTE by approximately 0.02–0.05 and 0.08–0.09 dex for the −2 and −1 dex stars, respectively. Interestingly, for Mn I in the infrared, Bergemann et al. (2019) report that 3D NLTE should be consistently higher than 1D NLTE by 0.15 dex for all analysed stars. However, as shown in Appendix A, no difference between the 1D LTE APOGEE and the 1D NLTE GALAH Mn abundances is observed, whilst the results in Bergemann et al. (2019) suggest a possible discrepancy of ∼0.15 dex at −1 dex and ∼0.2 dex at −2 dex (APOGEE being lower).

Although there is clear evidence that 1D LTE Mn abundances are too low at low metallicity, NLTE corrections depend sensitively on the details of the modelling and input data. Their dependence on effective temperature and surface gravity can be tested by requiring globular cluster stars have similar abundances. For example, Kirby et al. (2018) applied Cr and Co NLTE corrections to LTE measurements for globular cluster members but found the corrections introduced systematic trends that were not present in the LTE calculations. However, Kovalev et al. (2019) show how NLTE measurements of Fe, Mg, and Ti globular cluster stars do not increase the intracluster scatter. These studies suggest that it is far from trivial to apply corrections to the LTE abundances.

4.3 Comparison with Milky Way dwarf spheroidal galaxies

In a similar vein to our work, Kirby et al. (2019) and de los Reyes et al. (2020) have estimated the contributions of different SNe Ia to the five dwarf spheroidal galaxies (dSphs): Sculptor, Leo II, Draco, Sextans, and UMi. These isolated low-metallicity systems provide an alternative way to inspect chemical evolution of entire galaxies. Kirby et al. (2019) fitted linear models with a break to [X/Fe] versus [Fe/H] data with X = (Mg, Si, Ca, Cr, Fe, Co, and Ni) from which the yields of the supernovae could be computed. The advantage of this procedure is that the metallicity dependence of the supernovae yields can be more simply captured. However, unlike our procedure where there is a common set of evolutionary parameters (e.g. star formation, outflow), the fits for each abundance are independent. Based on the subsolar [Ni/Fe] of SNe Ia, Kirby et al. (2019) concluded there must be a significant contribution from sub-Chandrasekhar mass SNe Ia in these systems. de los Reyes et al. (2020) measured Mn abundances for Sculptor and fitted the same models as Kirby et al. (2019) to find $[Mn/Fe]_{Ia} = (-0.30 \pm 0.03)$ dex. These authors also suggest that systems with early concentrated star formation (such as Sculptor) have lower $[Mn/Fe]_{Ia}$, and hence higher fractions of sub-Chandrasekhar mass SNe Ia than systems with more extended star formation. This suggests that perhaps the dominant channel of Type Ia enrichment depends on delay time with Chandrasekhar mass systems dominating at late times.

In Fig. 7, we show our constraints for the *Gaia* Sausage alongside the constraints from the dSph models of Kirby et al. (2019) and de los Reyes et al. (2020) and the theoretical models of the previous section. Sculptor has a subsolar Type Ia [Mn/Fe] yield that is ∼0.1 dex lower than that for the *Gaia* Sausage. As for the *Gaia* Sausage result, the Sculptor result is consistent with a mixture of M_{Ch} and sub-M_{Ch} from the Kobayashi et al. (2020a) models or near 100 per cent sub-M_{Ch} from the Gronow et al. (2021b) or Pakmor et al. (2012) models. Similarly, both Sculptor and Leo II have subsolar $[Ni/Fe]_{Ia}$ like the *Gaia* Sausage. Draco and Sextans have lower $[Ni/Fe]_{Ia}$ still and UMi has the lowest $[Ni/Fe]_{Ia}$ consistent only with the sub-M_{Ch} yields. Cr presents a more complicated picture with all results (except that of UMi) around solar. This is consistent with almost any set of theoretical yields with the results of UMi suggesting a large fraction of sub-M_{Ch} or even pure deflagration models. The analysis from Palla (2021) demonstrates that Cr is more sensitive to the details of the explosion initialization and geometry, and so is more an indicator of different simulation setups. The α elements (Si and Ca) are subsolar for all dSphs and for the *Gaia* Sausage (again except for UMi which has a high [Si/Fe]). As with Cr, this is largely consistent with any set of theoretical SNe Ia yields.

4.4 Type Ia yields across a range of systems

The comparison with the dSph data in the previous section demonstrates that both the *Gaia* Sausage and dSphs have significant contribution from sub-M_{Ch} SNe Ia. However, there is also the suggestion of metallicity dependence in the Type Ia yields with Sculptor having a ∼0.1 dex lower [Mn/Fe] yield than *Gaia* Sausage, despite both systems having similar early bursts of star formation. To investigate the potential metallicity dependence of the Type Ia yields, we fit the simple analytic models to data from a wider range of systems. We consider APOGEE DR16 data for the MW bulge (selected as giants within 5° of the Galactic Centre), the LMC (fainter than $K_s = 12$ within 15° of the centre of the LMC and with a line-of-sight velocity cut), the SMC (fainter than $K_s = 12$ within 10° of the centre of the SMC and with a line-of-sight velocity cut), and the Sgr dSph (fainter than $H = 12$ within 5° of the centre of the Sgr, with a line-of-sight velocity cut and removing high-α *in situ* stars). We use similar quality cuts on the abundances to those in Section 2.3. Furthermore we take the dSph data from Kirby et al. (2018) combined with the Mn measurements from de los Reyes et al. (2020) for UMi, Canes Venatici I, Sculptor, Leo I, and Fornax.

We fit the analytic chemical evolution models to Mg, Si, Ca, Cr, Mn, and Ni adopting identical priors to those in Section 3 except for t_{max} and τ_{sfh} which are chosen on the basis of star formation history measurements (Gallart et al. 1999; Carrera et al. 2002; Harris & Zaritsky 2004, 2009; de Boer et al. 2012a,b; de Boer, Belokurov & Koposov 2015; Barbuy, Chiappini & Gerhard 2018). We display the results of the model fits in Fig. 8 along with the theoretical yields from the M_{Ch} models of Seitenzahl et al. (2013a) and Kobayashi et al. (2020a), and the sub-M_{Ch} 1 $M_\odot$ models from Kobayashi et al. (2020a) and Gronow et al. (2021a,b). The full set of model constraints is given in Table B2 and the model fits for the most massive systems are given in Fig. B1. We see that for all systems of lower metallicity than the SMC there is a weak gradient of [Mn/Fe] with metallicity. This gradient may be consistent with NLTE effects. Based on the discussion of Section 4.2, we have rerun the modelling with a [Mn/Fe] NLTE correction of −0.1[Fe/H], although this is possibly an overestimate of the effect. The shift in the results is shown by the small arrows in Fig. 8. It is clear NLTE effects could flatten the gradient at the metal-poor end. However, more robust is the difference

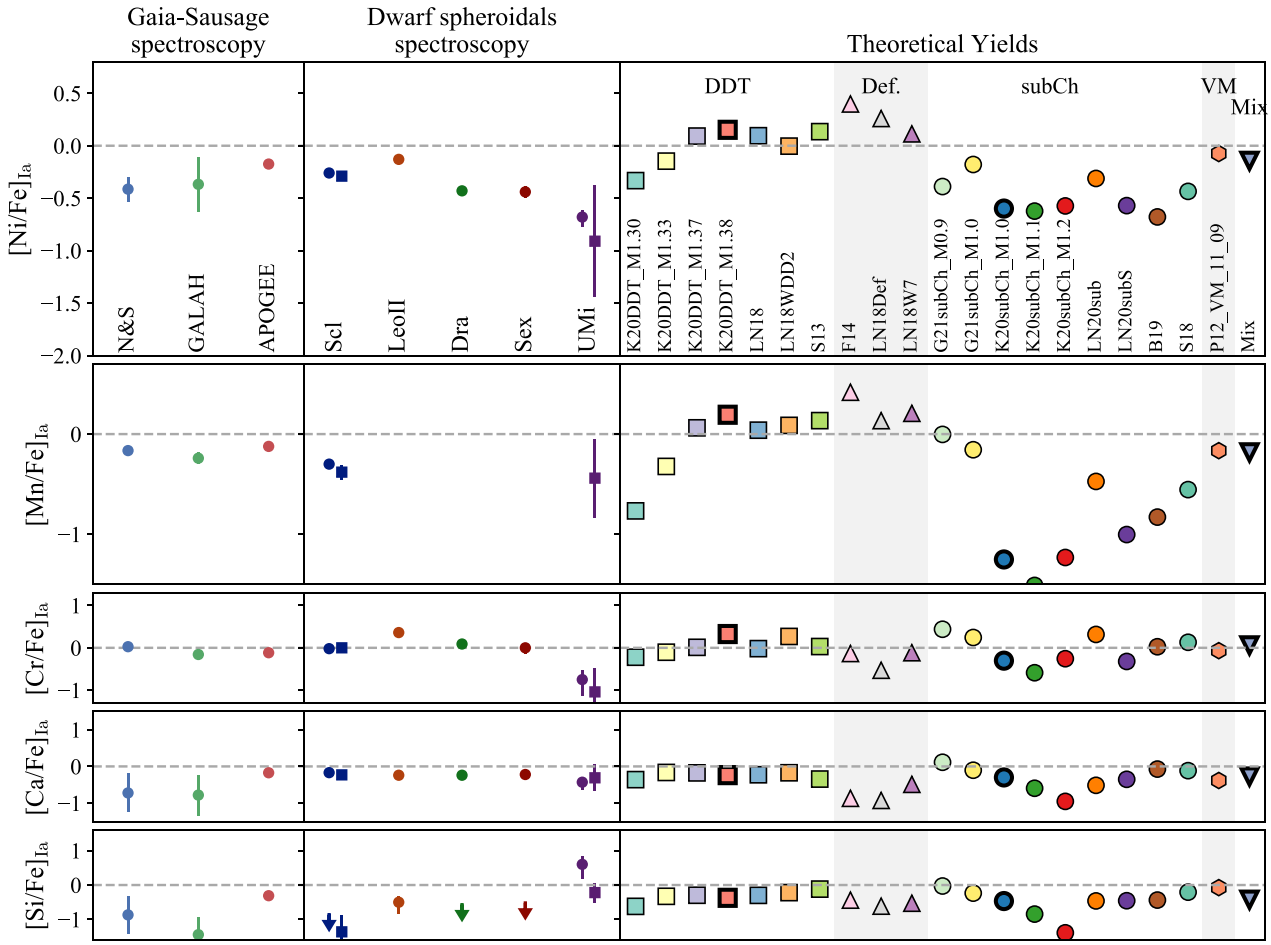

Figure 7. Comparison between the SNe Ia yields in the *Gaia* Sausage compared with (i) MW dSphs as measured by Kirby et al. (2019) and de los Reyes et al. (2020) for Mn (circles) and the model fits from Section 4.4 (squares), and (ii) theoretical Type Ia yields as defined in Table A1 (markers with thick black outlines show benchmark models that reproduce observed ^{56}Ni masses and the adopted mixture of the benchmark models). Subsolar [Mn/Fe] and [Ni/Fe] are observed in both the *Gaia* Sausage and the dSphs, indicating the importance of sub-Chandrasekhar mass SNe Ia in low-mass/low-metallicity systems.

in the yield required to explain the higher metallicity systems (MW bulge, LMC, Sgr) compared to the lower metallicity systems (e.g. *Gaia* Sausage). The lower metallicity systems cover a range of star formation histories (e.g. the early star formation of *Gaia* Sausage and Sculptor versus the more extended star formation history from Fornax) as do the high-metallicity systems (early star formation in the MW bulge versus extended, albeit bursty, star formation in the LMC). This suggests that although evolutionary differences may give rise to some variation at fixed metallicity (see later and de los Reyes et al. 2020), the main factor governing the Type Ia [Mn/Fe] yields is metallicity dependence.

4.4.1 *Modelling variants*

Before discussing the implications of our results, we will detail some caveats and model variants we have explored to test the robustness of our derived constraints.

Complex star formation histories. Several of these systems have more complicated star formation histories than can perhaps be captured by the linear–exponential star formation law of Weinberg et al. (2017). For example, the Magellanic Clouds are known to have relatively extended, bursty star formation histories, possibly linked to their mutual interaction (Harris & Zaritsky 2009; Nidever et al. 2020), or the MW bulge may have gone through bursts and quenching episodes (Lian et al. 2020). The models of Weinberg et al. (2017, see section 5.6) permit more complex star formation histories as linear sums of the analytic solutions (linear–exponential and exponential). Because of the linearity of the chemical evolution equations, the expressions for the *mass* of each element are just linear sums of the solutions for each component. We have considered more complex models of two linear–exponential terms with relative weight f_s, with one star formation law beginning at $t = 0$ and the other offset to begin at $t = t_0$, a free parameter. Each component has its own separate $\tau_{\rm sfh}$. Despite the added complexity, the constraints on the yields, particularly Mn and Ni, are very similar to those obtained with the single-component model. However, in general these models are much harder to sample from. Furthermore, removing the constraint that t_i follows the star formation law in the modelling produces significantly poorer matches to the metallicity distributions but the conclusions regarding [Mn/Fe]$_{\rm Ia}$ and [Ni/Fe]$_{\rm Ia}$ are unchanged. This suggests, despite the simplicity of the adopted star formation prescription and despite the sampling of the systems possibly being subject to selection effects that reshape the metallicity distributions, our results regarding the Mn and Ni abundances are robust to reasonable variations in the model star formation history parametrization. Note

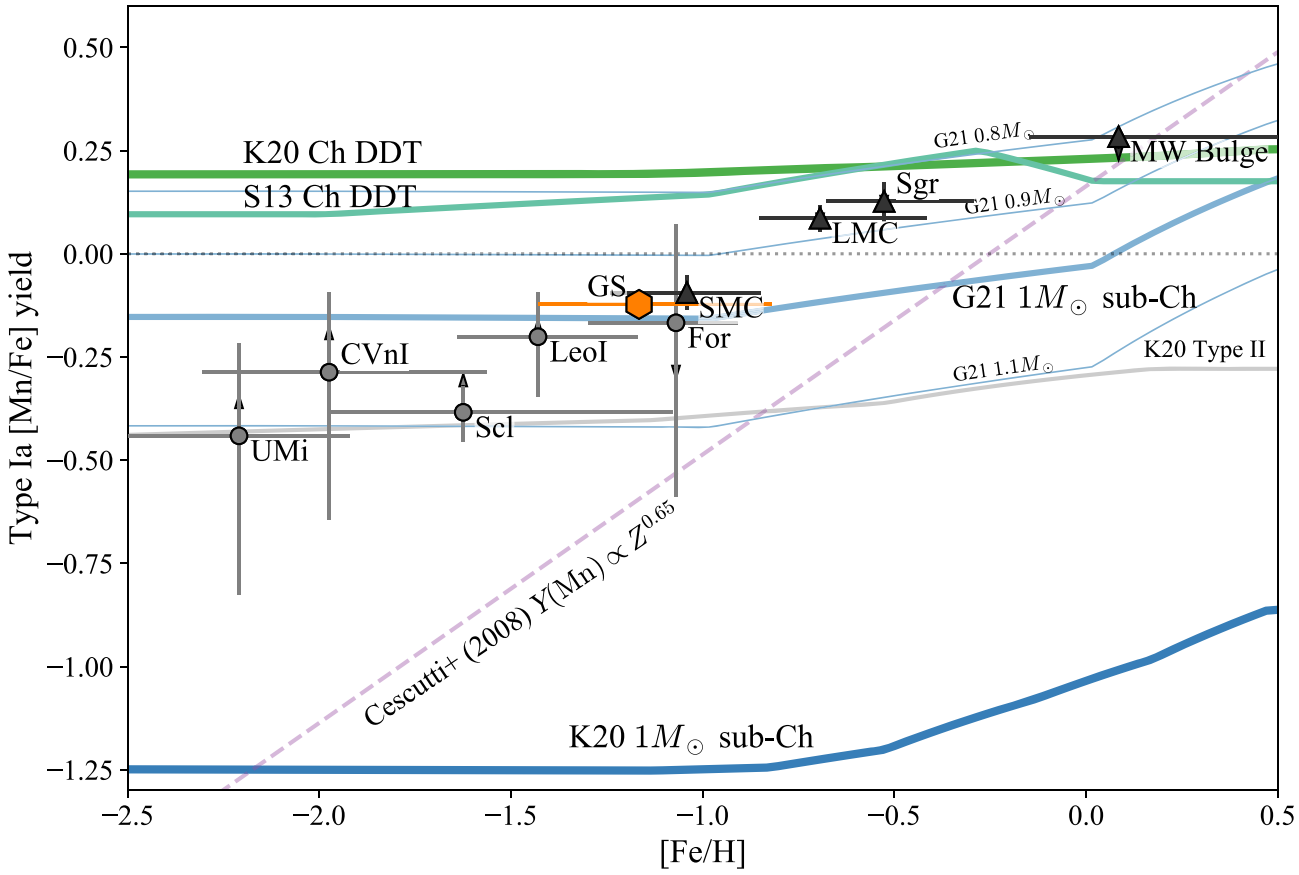

Figure 8. Inferred Type Ia [Mn/Fe] yield against metallicity for a range of environments. We show data for the MW bulge, the LMC and SMC, the *Gaia* Sausage (orange hexagon), and a number of dSphs. Vertical error bars show the uncertainty, whilst horizontal error bars give the metallicity spread of the considered stars (16th and 84th percentiles). The small arrows show the effect of correcting for NLTE effects by subtracting 0.1[Fe/H] from the individual abundances. We plot the $M_{\rm Ch}$ deflagration-to-detonation transition (DDT) metallicity-dependent yields from Seitenzahl et al. (2013a, S13 Ch DDT, dark green) and Kobayashi et al. (2020a, K20 Ch DDT, light green), and the sub-$M_{\rm Ch}$ double-detonation metallicity-dependent yields from Gronow et al. (2021a,b, G21 1 $M_\odot$ sub-Ch, thick light blue, and other masses in thinner lines) and Kobayashi et al. (2020a, K21 1 $M_\odot$ sub-Ch, dark blue). We also display in grey the Type II yields from Kobayashi et al. (2006) used in the Kobayashi et al. (2020b) models. The purple dashed line is the proposed metallicity dependence of the Type Ia Mn yields from Cescutti et al. (2008).

we are not arguing that the average Type Ia yields for each system do not correlate with the star formation history (see later discussion), rather our recovery of the average yields for each system is insensitive to modelling variations in the star formation history.

Metallicity-independent yields. A further caveat is that several of the studied systems (in particular the MW bulge) span a large range in metallicity such that the metallicity-independent yields prescription of the analytic models is possibly questionable. For example, in the case of the MW bulge, the simplistic models fail to perfectly capture the morphology of the nearly linearly rising [Mn/Fe] versus [Fe/H]. This is indicative of the need for metallicity-dependent yields for this system (Gronow et al. 2021b). For both of these reasons, our measurements should be considered as average SNe Ia yields corresponding approximately to the metallicity at which the bulk of the stars were formed.

Metallicity-dependent Type II yields may also play a role and, as discussed, these are not well incorporated in our modelling framework. In Fig. 8, we show the weak metallicity dependence of Type II yields from the models of Kobayashi et al. (2006, 2020b) where the [Mn/Fe] difference between [Fe/H] $= -1$ and 0 dex is $\sim$0.1 dex. Other Type II supernovae yields give $\sim$0.13 dex (Chieffi & Limongi 2004), $\sim$0.27 dex (Woosley & Weaver 1995; Pignatari et al. 2016; Ritter et al. 2018), or as large as $\sim$0.6 dex (Limongi & Chieffi 2018; Prantzos et al. 2018) for this quantity. Such a large variation could in principle explain the [Mn/Fe] trend for the MW bulge. However, the maximum $[{\rm Mn/Fe}]_{\rm II}$ yield at solar metallicity for any model is $\sim$0.1 dex (Limongi & Chieffi 2018; Prantzos et al. 2018). Assuming the same relative contribution to stars of solar metallicity from Type Ia and Type II yields as found in the default model fit, $[{\rm Mn/Fe}]_{\rm Ia}$ would be lowered from 0.28 to $\sim$0.07 dex in this case. Even in this extreme case, supersolar Type Ia yields are required for high-metallicity systems. As a further test, we incorporated a form of metallicity-dependent Type II yields in our models by including a different η parameter for each element. As referenced in Section 3, a Type II yield, $m_j^{\rm II}$, which depends linearly on the current mass fraction of element j, Z_j, relative to solar is equivalent to changing the depletion time-scale $\tau_{\rm dep}$ for this element. We included a unit normal prior on the gradient of $m_j^{\rm II}/m_j^{\rm II}(Z_j = 0)$ with respect to Z_j (consistent with the spread from the theoretical yields). Furthermore, we enforced the yield for a mass fraction 10 times solar to be positive. This produced no difference in $[{\rm Mn/Fe}]_{\rm Ia}$ for systems with [Fe/H] < -1 dex (including the *Gaia* Sausage). For the LMC, Sgr, and the MW bulge, $[{\rm Mn/Fe}]_{\rm Ia}$ was significantly lower (-0.09, -0.06, and -0.18 dex, respectively) but, in the cases of the MW bulge and

the LMC, only by invoking unphysically steep Type II metallicity gradients such that $[Mn/Fe]_{II} \sim 0.3$–0.5 dex at solar metallicity. Thus it seems that although metallicity-dependent Type II yields could contribute to the interpretation of the data, they will only weakly flatten the gradient seen in Fig. 8 and the observation that the MW bulge data require SNe Ia Mn yields inconsistent with the lower metallicity systems (e.g. *Gaia* Sausage) is robust.

Tensions with priors. From inspecting Table B2, there are a few parameter constraints that are in tension with our adopted priors. In particular, $\log_{10} m_{Fe}$ for the Type II and Type Ia channels are in some instances much higher than the priors (e.g. the MW bulge and the LMC). Running models with much tighter priors on these quantities (0.004 dex) produces very similar results for $[X/Fe]_{Ia,\,II}$ and by eye a similar quality of fit to the abundance trends. This is typically achieved through lowering t_D such that it pushes against the 40 Myr lower bound and is consistent with very prompt SNe Ia exploding soon after their progenitor star becomes a WD. Another quirk of our modelling is the low η constraint for the MW bulge (consistent with zero) indicating very low outflow. Allowing η to be negative produces a constraint of $\eta = (-0.15 \pm 0.12)$, which, as discussed previously, we could physically interpret as a Type II iron yield increasing with metallicity. Relaxing the positivity constraint on η does not affect the inferred abundances.

We conclude that, despite some deficiencies in our modelling approach, the main results that we focus on are robust to reasonable variations of the model. This is further corroborated by the results of our models for Sculptor and UMi compared to the models of Kirby et al. (2019) and de los Reyes et al. (2020) as shown in Fig. 7, demonstrating the good agreement between the two modelling frameworks. We now discuss the meaning of these results.

4.4.2 *Metallicity-dependent Type Ia yields*

Metallicity-dependent Type Ia [Mn/Fe] yields have long been proposed as an explanation for the rising [Mn/Fe] versus [Fe/H] for MW stars (e.g. Cescutti et al. 2008; Weinberg et al. 2019). There are two possible routes for how such a metallicity dependence could arise. If we simply consider two different Type Ia channels, it could either be that the individual [Mn/Fe] yields from the two channels are metallicity dependent, or the relative contribution from the two channels is metallicity dependent. Both the models of Kobayashi et al. (2020a) and Gronow et al. (2021b) demonstrate that metallicity dependence of $[Mn/Fe]_{Ia}$ can be significant for sub-M_{Ch} models above $[Fe/H] \approx -1$ dex. This effect is driven by the neutron excess for more metal-rich models altering the relative abundance of iron-group elements from incomplete silicon burning (typically during He detonation). On the other hand, the $[Mn/Fe]_{Ia}$ for the M_{Ch} DDT models (Seitenzahl et al. 2013a; Kobayashi et al. 2020a) are much less metallicity dependent as in this case ^{55}Co is typically produced in nuclear statistical equilibrium so is sensitive more to the neutron fraction from electron capture and less to the initial composition. Additionally, pre-explosion simmering (Piro & Bildsten 2008) should make the pre-explosion neutron abundance more insensitive to the initial metallicity. As highlighted by Gronow et al. (2021b), the rising trend of [Mn/Fe] versus [Fe/H] for the MW then requires significant metallicity-dependent sub-M_{Ch} contributions. On the other hand, there are theoretical arguments that the M_{Ch} channel becomes more significant for higher metallicity systems as winds are required to grow WDs stably to M_{Ch} which are more effective at higher metallicity (Kobayashi & Nomoto 2009). In the recent MW models of Kobayashi et al. (2020a, fig. 14), M_{Ch} SNe Ia only begin contributing after $t = 4$ Gyr when the Galaxy is enriched to around $[Fe/H] = -1$ dex. However, we must also consider the birth and evolutionary properties of binary systems with metallicity. Recently, it has become clear that binarity is more common at low metallicities (Moe, Kratter & Badenes 2019) possibly due to increased fragmentation at lower metallicity caused by lower dust opacities and enhanced gas cooling through dust coupling. Whether such an effect could differentially affect the two channels is not clear. Additionally, as highlighted by Ruiter (2020), mass loss is more effective at higher metallicities. At very low metallicity ($[Fe/H] \approx -2$ dex) low mass loss can produce fewer single-degenerate channel SNe Ia as oxygen–neon (ONe) WDs are formed preferentially. At higher metallicities, increased mass loss over the stellar lifetime can change the evolutionary pathway of a binary, make the Chandrasekhar mass harder to reach or prevent contact and subsequent stable mass transfer (as highlighted above). These three effects can significantly alter the predicted rates of different channels.

4.4.3 *Star-formation-history-dependent Type Ia yields*

Finally, we consider the possibility that some of the variation we see is due to different star formation histories in the systems. There is a well-studied trend for more massive galaxies to host intrinsically fainter SNe Ia events (e.g. Howell et al. 2009), which could be related to either age or metallicity effects. One plausible explanation is that the more massive systems host longer delay time SNe Ia, which could arise from lower mass progenitor systems in the sub-M_{Ch} scenario (Howell 2001) although disentangling age and metallicity effects is non-trivial. This observation would appear at odds with the theory of increased dominance of M_{Ch} systems in higher metallicity environments, although crucially the host galaxy correlations are against gas-phase metallicity which could be quite different from the progenitor metallicity depending on the star formation history. In the sub- M_{Ch} scenario there is the additional parameter of the progenitor mass. As noted previously, the models of Kobayashi et al. (2020a) show weak mass dependence at fixed metallicity, whilst there is more significant variation with mass in the Gronow et al. (2021a,b) models. In Fig. 8, we show the 0.8, 0.9, and 1.1 $M_\odot$ core mass models from Gronow et al. (2021a,b) as thin lines. At fixed metallicity, the [Mn/Fe] yield increases with decreasing core mass. This is mostly driven by the correlation of ^{56}Ni mass with core mass, as the mass of Mn is linked to the He detonation at the lower density core/shell interface and is more constant with core mass. We observe that systems such as the LMC or Sgr with perhaps more extended star formation histories may be entirely consistent with 100 per cent sub-M_{Ch} models but of lower mass. Such a picture would be in line with the supernovae population studies. It appears from [Mn/Fe] alone that breaking the degeneracy between core mass and metallicity is not trivial.

Flörs et al. (2020) have used spectroscopic observations of the ratio ^{58}Ni to ^{56}Ni to infer the mass of individual SNe Ia. As a neutron-rich species, the ^{58}Ni abundance depends on neutron fraction so is higher for higher mass, higher density WDs (Timmes, Brown & Truran 2003). This difference in behaviour with mass for [Ni/Fe] compared to [Mn/Fe] allows breaking of the degeneracy when using only [Mn/Fe]. In Fig. 9, we display the joint constraints on Type Ia [Mn/Fe] and [Ni/Fe] yields for the six best constrained systems we have analysed alongside the sub-M_{Ch} models from Gronow et al. (2021a,b). We observe that, despite higher Type Ia [Mn/Fe] abundance in the LMC and Sgr compared to the *Gaia* Sausage, the [Ni/Fe] abundance in these systems is lower than that for the

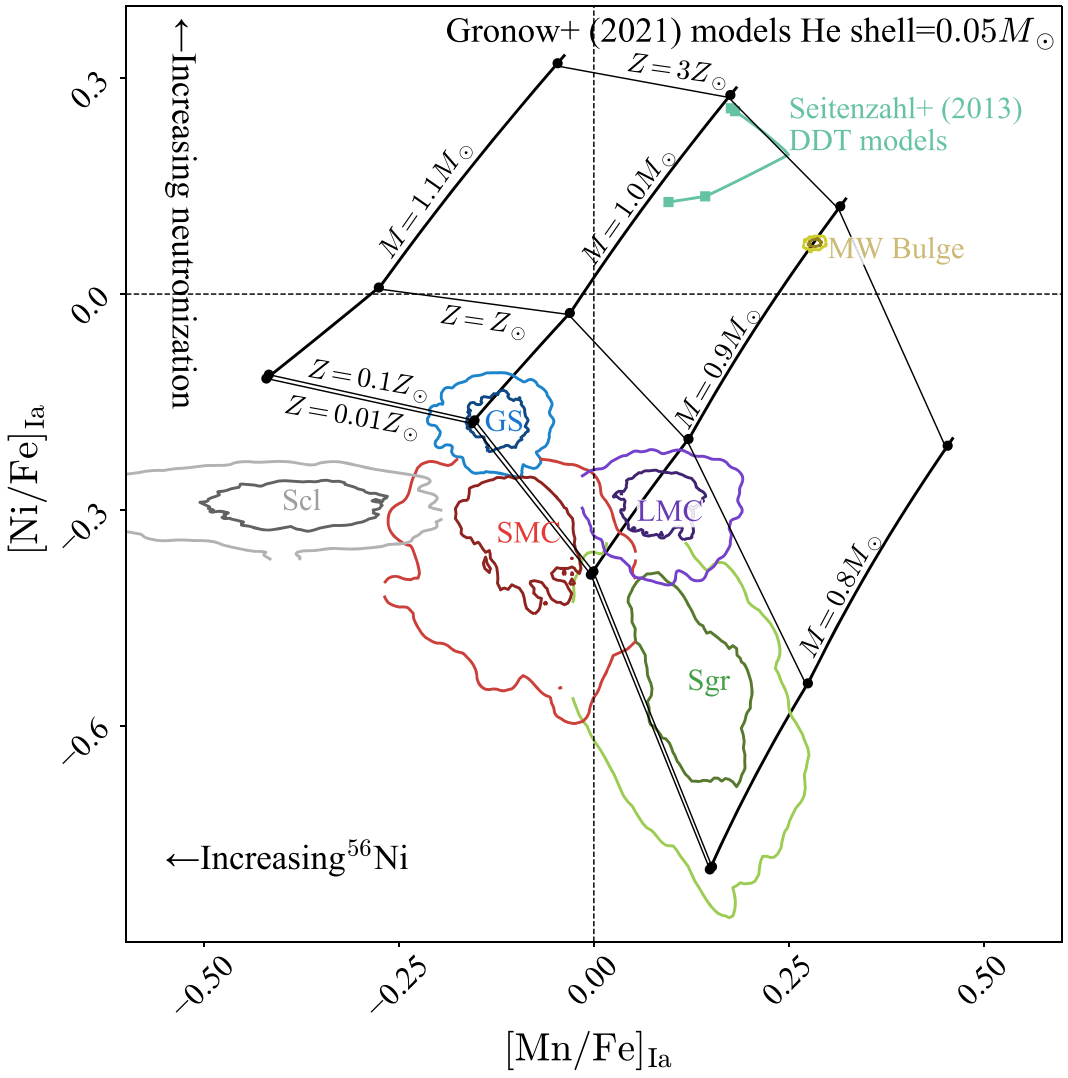

Figure 9. Joint constraints on Type Ia [Mn/Fe] and [Ni/Fe] yields for a range of Local Group systems together with the sub-M_{Ch} models of Gronow et al. (2021a,b, black) and the M_{Ch} DDT models of Seitenzahl et al. (2013a, green). The yields are functions of both core mass and metallicity of the sub-M_{Ch} progenitor. Increased mass increases ^{56}Ni production (and hence Fe) whilst Mn remains constant (as it is formed in lower density regions at the core–shell interface), and increases the neutronization elevating the abundance of neutron-rich ^{58}Ni.

Gaia Sausage and appears more consistent with 0.8 or 0.9 $M_\odot$ core mass models, in line with our expectation from their more extended star formation history. We have chosen the 0.05 $M_\odot$ He shell mass models from Gronow et al. (2021a,b) but similar conclusions hold for other He shell mass models although there is more variance in the abundances for lower (0.8, 0.9 $M_\odot$) core mass models with varying shell mass. To draw firmer conclusions requires a more detailed modelling of the star formation histories of the systems and the DTDs with WD mass, but the combined constraints from [Mn/Fe] and [Ni/Fe] appear to provide a route to more strongly constrain the SNe Ia progenitor scenario and could even point towards sub-M_{Ch} dominance in all systems.

Based on the currently available theoretical models, the combination of results from the different systems suggests an increasing significance of M_{Ch} explosions with increasing metallicity, although the differences between different theoretical models hint there may be a model where the metallicity dependence is explained entirely by sub-M_{Ch} explosions, possibly with a distribution of masses related to the star formation history of the system. The plane of [Mn/Fe] versus [Ni/Fe] seems ideal to distinguish these scenarios.

5 CONCLUSIONS

The range of different SNe Ia scenarios is distinguished by different nucleosynthetic yields, which are in turn imprinted in the chemical abundances of stars. SNe Ia channels potentially vary with the mass, metallicity, IMF, and star formation history of the host systems which could have profound consequences on the use of SNe Ia as cosmological probes. However, high-quality resolved stellar spectroscopic abundances are available only for the MW and several Local Group dwarf galaxies. Recently, it has been discovered that a substantial fraction of the MW's halo consists of a population of kinematically and chemically distinct stars consistent with originating from a significant merger, dubbed the *Gaia* Sausage, early in the life of the MW. This gives us a unique probe into a low-metallicity, early Universe galaxy using sets of bright local tracers.

We have taken three samples of *Gaia* Sausage stars from NS10, GALAH DR3 (Buder et al. 2021), and APOGEE DR16 (Ahumada et al. 2020) for which high-dimensional chemical data are available (eight+ abundances), and fitted their chemical-space distributions with the simple analytic chemical evolution models of Weinberg et al. (2017) to measure the abundance signatures of SNe Ia. We find the downturning [α/Fe] sequence indicative of the onset of SNe Ia is accompanied by a relatively flat [Mn/Fe] and weakly declining [Ni/Fe] trend indicating low production in SNe Ia (~-0.15 and ~-0.3 dex, respectively). Comparison with theoretical nucleosynthetic yields for SNe Ia exploded as $M_{\rm Ch}$ pure deflagrations, $M_{\rm Ch}$ DDT, and double-detonation sub-$M_{\rm Ch}$ demonstrate such behaviour is only possible with a significant ($\gtrsim$60 per cent) contribution of sub-$M_{\rm Ch}$ systems, with some theoretical calculations implying near 100 per cent sub-$M_{\rm Ch}$ systems. This corroborates findings from dwarf galaxies of the Local Group.

Finally, we concluded our study with a combined analysis of several systems with varying star formation histories and metallicity distributions (MW bulge, Magellanic Clouds, *Gaia* Sausage, and dSphs). We found to reproduce the chemical enrichment of all of these systems requires a metallicity-dependent Type Ia [Mn/Fe] yield. Only sub-$M_{\rm Ch}$ models have significant metallicity-dependent yields. This then indicates either

(i) a significant contribution from sub-$M_{\rm Ch}$ SNe Ia in all systems, possibly with variation in the WD mass distribution with star formation history which could be elucidated using a combination of [Ni/Fe] and [Mn/Fe] measurements, or

(ii) an enhancement of the $M_{\rm Ch}$ channel at higher metallicity, possibly due to stabilizing winds allowing WD growth to the Chandrasekhar mass.

We close by reflecting on the implications of our work on using SNe Ia as cosmological probes. The understanding of the progenitors of SNe Ia is an important part of using these objects as standard candles. However, the success in their use has arisen from the ability to standardize the variety of observed light curves, even despite an understanding of what drives the variation. From the $M_{\rm Ch}$ perspective, the free parameter is perhaps the time a deflagration flame transitions into a detonation wave (Blondin et al. 2013), whilst in the sub-$M_{\rm Ch}$ picture, it is the mass of the WD. In both cases, however, the primary driver in light-curve variation is then the ^{56}Ni production which gives rise to the width–luminosity relation (Scalzo et al. 2014). Beyond this, there is an intrinsic scatter of $\sim$0.15 mag in SNe Ia luminosities, the cause of which is not understood. If the residual depends on the progenitor scenario, and possibly more crucially the host galaxy properties, there is scope to improve the calibrations and remove potential systematics (e.g. Sullivan et al. 2010). For instance, several studies (e.g. Howell et al. 2009; Kelly et al. 2010; Scalzo et al. 2014) have demonstrated SNe Ia in less massive galaxies tend to be brighter (even after calibrating the light curves), reflecting possible age (Childress, Wolf & Zahid 2014) or metallicity effects (Timmes et al. 2003) on the progenitors. Such correlations favour the sub-$M_{\rm Ch}$ channel where lower mass older WDs could explode at longer delay times producing lower luminosity SNe Ia (Howell 2001). Such studies are concerned with the properties of observed supernovae, whilst here we are only sensitive to the SNe Ia that enrich future star-forming gas, and furthermore, supernovae observations are unable to probe the gas metallicity when the progenitor was born. For these reasons, our results are complementary to SNe Ia population studies and taken together give a route into further understanding the SNe Ia progenitor properties with both metallicity and star formation history of the host.

ACKNOWLEDGEMENTS

The authors would like to thank Chiaki Kobayashi for providing the yields from the work of Kobayashi et al. (2020a). JLS acknowledges support from the Royal Society (URF\R1\191555). Thanks to Richard Ellis for suggesting investigating supernovae scenarios using *Gaia* Sausage data.

This work made use of the Heidelberg Supernova Model Archive (HESMA), https://hesma.h-its.org. This paper made use of NUMPY (van der Walt, Colbert & Varoquaux 2011), SCIPY (Virtanen et al. 2020), MATPLOTLIB (Hunter 2007), SEABORN (Waskom et al. 2021), ASTROPY (Astropy Collaboration et al. 2013; Price-Whelan et al. 2018), CHAINCONSUMER (Hinton 2016), and STAN (Carpenter et al. 2017). This work has made use of data from the European Space Agency (ESA) mission *Gaia* (https://www.cosmos.esa.int/gaia), processed by the *Gaia* Data Processing and Analysis Consortium (DPAC, https://www.cosmos.esa.int/web/gaia/dpac/consortium). Funding for the DPAC has been provided by national institutions, in particular the institutions participating in the *Gaia* Multilateral Agreement.

This work made use of the Third Data Release of the GALAH Survey (Buder et al. 2021). The GALAH Survey is based on data acquired through the Australian Astronomical Observatory, under programs: A/2013B/13 (The GALAH pilot survey); A/2014A/25, A/2015A/19, A2017A/18 (The GALAH survey phase 1); A2018A/18 (Open clusters with HERMES); A2019A/1 (Hierarchical star formation in Ori OB1); A2019A/15 (The GALAH survey phase 2); A/2015B/19, A/2016A/22, A/2016B/10, A/2017B/16, A/2018B/15 (The HERMES-TESS program); and A/2015A/3, A/2015B/1, A/2015B/19, A/2016A/22, A/2016B/12, A/2017A/14 (The HERMES K2-follow-up program). We acknowledge the traditional owners of the land on which the AAT stands, the Gamilaraay people, and pay our respects to elders past and present. This paper includes data that have been provided by AAO Data Central (datacentral.aao.gov.au).

Funding for the Sloan Digital Sky Survey IV (SDSS-IV) has been provided by the Alfred P. Sloan Foundation, the U.S. Department of Energy, Office of Science, and the Participating Institutions. SDSS-IV acknowledges support and resources from the Center for High Performance Computing at the University of Utah. The SDSS website is www.sdss.org. SDSS-IV is managed by the Astrophysical Research Consortium for the Participating Institutions of the SDSS Collaboration including the Brazilian Participation Group, the Carnegie Institution for Science, Carnegie Mellon University, Center for Astrophysics | Harvard & Smithsonian, the Chilean Participation Group, the French Participation Group, Instituto de Astrofísica de Canarias, The Johns Hopkins University, Kavli Institute for the Physics and Mathematics of the Universe (IPMU)/University of Tokyo, the Korean Participation Group, Lawrence Berkeley National Laboratory, Leibniz Institut für Astrophysik Potsdam (AIP), Max-Planck-Institut für Astronomie (MPIA Heidelberg), Max-Planck-Institut für Astrophysik (MPA Garching), Max-Planck-Institut für Extraterrestrische Physik (MPE), National Astronomical Observatories of China, New Mexico State University, New York University, University of Notre Dame, Observatário Nacional/MCTI, The Ohio State University, Pennsylvania State University, Shanghai Astronomical Observatory, United Kingdom Participation Group, Universidad Nacional Autónoma de México, University of Arizona, University of Colorado Boulder, University of Oxford, University of Portsmouth, University of Utah, University of Virginia, University of Washington, University of Wisconsin, Vanderbilt University, and Yale University.

DATA AVAILABILITY

All of the data used in this work is in the public domain.

REFERENCES

Aguado D. S. et al., 2021, ApJ, 908, L8
Ahumada R. et al., 2020, ApJS, 249, 3
Amarsi A. M. et al., 2020, A&A, 642, A62
Arnett W. D., 1969, Ap&SS, 5, 180
Arnett W. D., Truran J. W., Woosley S. E., 1971, ApJ, 165, 87
Asplund M., Grevesse N., Sauval A. J., Scott P., 2009, ARA&A, 47, 481
Astropy Collaboration et al., 2013, A&A, 558, A33
Badenes C., Borkowski K. J., Bravo E., 2005, ApJ, 624, 198
Barbuy B., Chiappini C., Gerhard O., 2018, ARA&A, 56, 223
Battistini C., Bensby T., 2015, A&A, 577, A9
Belokurov V., Erkal D., Evans N. W., Koposov S. E., Deason A. J., 2018, MNRAS, 478, 611
Belokurov V., Sanders J. L., Fattahi A., Smith M. C., Deason A. J., Evans N. W., Grand R. J. J., 2020, MNRAS, 494, 3880
Benz W., Bowers R. L., Cameron A. G. W., Press W. H., 1990, ApJ, 348, 647
Bergemann M., Gehren T., 2008, A&A, 492, 823
Bergemann M. et al., 2019, A&A, 631, A80
Blondin S., Dessart L., Hillier D. J., Khokhlov A. M., 2013, MNRAS, 429, 2127
Bonaca A. et al., 2020, ApJ, 897, L18
Bovy J., 2015, ApJS, 216, 29
Bravo E., Badenes C., Martínez-Rodríguez H., 2019, MNRAS, 482, 4346
Buder S. et al., 2021, MNRAS, 506, 150
Carpenter B. et al., 2017, J. Stat. Softw., 76, 1
Carrera R., Aparicio A., Martínez-Delgado D., Alonso-García J., 2002, AJ, 123, 3199
Cescutti G., Matteucci F., Lanfranchi G. A., McWilliam A., 2008, A&A, 491, 401
Chabrier G., 2003, PASP, 115, 763
Chieffi A., Limongi M., 2004, ApJ, 608, 405
Childress M. J., Wolf C., Zahid H. J., 2014, MNRAS, 445, 1898
Deason A. J., Belokurov V., Evans N. W., Johnston K. V., 2013, ApJ, 763, 113
de Boer T. J. L. et al., 2012a, A&A, 539, A103
de Boer T. J. L. et al., 2012b, A&A, 544, A73
de Boer T. J. L., Belokurov V., Koposov S., 2015, MNRAS, 451, 3489
de los Reyes M. A. C., Kirby E. N., Seitenzahl I. R., Shen K. J., 2020, ApJ, 891, 85
Dias W. S., Alessi B. S., Moitinho A., Lépine J. R. D., 2002, A&A, 389, 871
Eitner P., Bergemann M., Larsen S., 2019, A&A, 627, A40
Eitner P., Bergemann M., Hansen C. J., Cescutti G., Seitenzahl I. R., Larsen S., Plez B., 2020, A&A, 635, A38
Evans N. W., 2020, in Valluri M., Sellwood J. A., eds, Proc. IAU Symp. Vol. 353, Galactic Dynamics in the Era of Large Surveys. Cambridge Univ. Press, Cambridge, p. 113
Feuillet D. K., Feltzing S., Sahlholdt C. L., Casagrande L., 2020, MNRAS, 497, 109
Fink M., Röpke F. K., Hillebrandt W., Seitenzahl I. R., Sim S. A., Kromer M., 2010, A&A, 514, A53
Fink M. et al., 2014, MNRAS, 438, 1762
Flörs A. et al., 2020, MNRAS, 491, 2902
Foley R. J. et al., 2013, ApJ, 767, 57
Gaia Collaboration et al., 2016, A&A, 595, A1
Gaia Collaboration et al., 2021, A&A, 649, A1
Gallart C., Freedman W. L., Aparicio A., Bertelli G., Chiosi C., 1999, AJ, 118, 2245
García Pérez A. E. et al., 2016, AJ, 151, 144
Gilfanov M., Bogdán Á., 2010, Nature, 463, 924
Gronow S., Collins C. E., Sim S. A., Roepke F. K., 2021a, A&A, 649, A155
Gronow S., Cote B., Lach F., Seitenzahl I. R., Collins C. E., Sim S. A., Roepke F. K., 2021b, preprint (arXiv:2103.14050)
Guillochon J., Dan M., Ramirez-Ruiz E., Rosswog S., 2010, ApJ, 709, L64
Gunn J. E. et al., 2006, AJ, 131, 2332
Harris W. E., 1996, AJ, 112, 1487
Harris J., Zaritsky D., 2004, AJ, 127, 1531
Harris J., Zaritsky D., 2009, AJ, 138, 1243
Helmi A., Babusiaux C., Koppelman H. H., Massari D., Veljanoski J., Brown A. G. A., 2018, Nature, 563, 85
Hillebrandt W., Niemeyer J. C., 2000, ARA&A, 38, 191
Hinton S. R., 2016, J. Open Source Softw., 1, 00045
Hoeflich P., Khokhlov A., 1996, ApJ, 457, 500
Howell D. A., 2001, ApJ, 554, L193
Howell D. A. et al., 2009, ApJ, 691, 661
Hunter J. D., 2007, Comput. Sci. Eng., 9, 90
Iben I., Jr, Tutukov A. V., 1984, ApJS, 54, 335
Iwamoto K., Brachwitz F., Nomoto K., Kishimoto N., Umeda H., Hix W. R., Thielemann F.-K., 1999, ApJS, 125, 439
Jönsson H. et al., 2018, AJ, 156, 126
Jönsson H. et al., 2020, AJ, 160, 120
Kelly P. L., Hicken M., Burke D. L., Mandel K. S., Kirshner R. P., 2010, ApJ, 715, 743
Kepler S. O., Kleinman S. J., Nitta A., Koester D., Castanheira B. G., Giovannini O., Costa A. F. M., Althaus L., 2007, MNRAS, 375, 1315
Khokhlov A. M., 1991, A&A, 245, 114
Kim Y. K., Lee Y. S., Beers T. C., Koo J.-R., 2021, ApJ, 911, L21
Kirby E. N., Xie J. L., Guo R., Kovalev M., Bergemann M., 2018, ApJS, 237, 18
Kirby E. N. et al., 2019, ApJ, 881, 45
Kobayashi C., Nomoto K., 2009, ApJ, 707, 1466
Kobayashi C., Umeda H., Nomoto K., Tominaga N., Ohkubo T., 2006, ApJ, 653, 1145
Kobayashi C., Leung S.-C., Nomoto K., 2020a, ApJ, 895, 138
Kobayashi C., Karakas A. I., Lugaro M., 2020b, ApJ, 900, 179
Kos J. et al., 2017, MNRAS, 464, 1259
Kovalev M., Bergemann M., Ting Y.-S., Rix H.-W., 2019, A&A, 628, A54
Kromer M., Sim S. A., Fink M., Röpke F. K., Seitenzahl I. R., Hillebrandt W., 2010, ApJ, 719, 1067
Kromer M. et al., 2013, ApJ, 778, L18
Kromer M. et al., 2016, MNRAS, 459, 4428
Kroupa P., 2001, MNRAS, 322, 231
Kroupa P., Tout C. A., Gilmore G., 1993, MNRAS, 262, 545
Lach F., Röpke F. K., Seitenzahl I. R., Coté B., Gronow S., Ruiter A. J., 2020, A&A, 644, A118
Lane J. M. M., Bovy J., Mackereth J. T., 2021, preprint (arXiv:2106.09699)
Leung H. W., Bovy J., 2019, MNRAS, 489, 2079
Leung S.-C., Nomoto K., 2018, ApJ, 861, 143
Leung S.-C., Nomoto K., 2020, ApJ, 888, 80
Lian J. et al., 2020, MNRAS, 497, 3557
Limongi M., Chieffi A., 2018, ApJS, 237, 13
Mackereth J. T. et al., 2019, MNRAS, 482, 3426
McMillan P. J., 2017, MNRAS, 465, 76
McWilliam A., Piro A. L., Badenes C., Bravo E., 2018, ApJ, 857, 97
Majewski S. R. et al., 2017, AJ, 154, 94
Maoz D., Mannucci F., 2012, Publ. Astron. Soc. Aust., 29, 447
Maoz D., Mannucci F., Nelemans G., 2014, ARA&A, 52, 107
Matsuno T., Hirai Y., Tarumi Y., Hotokezaka K., Tanaka M., Helmi A., 2021, A&A, 650, A110
Moe M., Kratter K. M., Badenes C., 2019, ApJ, 875, 61
Myeong G. C., Evans N. W., Belokurov V., Sanders J. L., Koposov S. E., 2018, ApJ, 863, L28
Myeong G. C., Vasiliev E., Iorio G., Evans N. W., Belokurov V., 2019, MNRAS, 488, 1235
Naidu R. P., Conroy C., Bonaca A., Johnson B. D., Ting Y.-S., Caldwell N., Zaritsky D., Cargile P. A., 2020, ApJ, 901, 48
Nidever D. L. et al., 2020, ApJ, 895, 88
Nissen P. E., Schuster W. J., 2010, A&A, 511, L10(NS10)
Nissen P. E., Schuster W. J., 2011, A&A, 530, A15
Nomoto K., Leung S.-C., 2018, Space Sci. Rev., 214, 67
Nomoto K., Thielemann F. K., Yokoi K., 1984, ApJ, 286, 644
North P. et al., 2012, A&A, 541, A45

Osorio Y., Allende Prieto C., Hubeny I., Mészáros S., Shetrone M., 2020, A&A, 637, A80
Pakmor R., Kromer M., Röpke F. K., Sim S. A., Ruiter A. J., Hillebrandt W., 2010, Nature, 463, 61
Pakmor R., Kromer M., Taubenberger S., Sim S. A., Röpke F. K., Hillebrandt W., 2012, ApJ, 747, L10
Palla M., 2021, MNRAS, 503, 3216
Perlmutter S. et al., 1999, ApJ, 517, 565
Phillips M. M., 1993, ApJ, 413, L105
Pignatari M. et al., 2016, ApJS, 225, 24
Piro A. L., Bildsten L., 2008, ApJ, 673, 1009
Prantzos N., Abia C., Limongi M., Chieffi A., Cristallo S., 2018, MNRAS, 476, 3432
Price-Whelan A. M. et al., 2018, AJ, 156, 123
Pskovskii I. P., 1977, SvA, 21, 675
Riess A. G. et al., 1998, AJ, 116, 1009
Ritter C., Herwig F., Jones S., Pignatari M., Fryer C., Hirschi R., 2018, MNRAS, 480, 538
Ruiter A. J., 2020, Barstow M. A., Kleinman S. J., Provencal J. L., Ferrario L., eds, Proc. IAU Symp. Vol. 357, White Dwarfs as Probes of Fundamental Physics: Tracers of Planetary, Stellar and Galactic Evolution. Cambridge Univ. Press, Cambridge, p. 1
Ruiter A. J., Belczynski K., Fryer C., 2009, ApJ, 699, 2026
Salpeter E. E., 1955, ApJ, 121, 161
Scalzo R. A., Ruiter A. J., Sim S. A., 2014, MNRAS, 445, 2535
Seitenzahl I. R., Townsley D. M., 2017, in Alsabti A., Murdin P., eds, Handbook of Supernovae. Springer, Cham, Switzerland, p. 1
Seitenzahl I. R. et al., 2013a, MNRAS, 429, 1156
Seitenzahl I. R., Cescutti G., Röpke F. K., Ruiter A. J., Pakmor R., 2013b, A&A, 559, L5
Shappee B. J., Piro A. L., Stanek K. Z., Patel S. G., Margutti R. A., Lipunov V. M., Pogge R. W., 2018, ApJ, 855, 6
Sheinis A. et al., 2015, J. Astron. Telesc. Instrum. Syst., 1, 035002
Shen K. J., Kasen D., Miles B. J., Townsley D. M., 2018a, ApJ, 854, 52
Shen K. J. et al., 2018b, ApJ, 865, 15
Sim S. A., Röpke F. K., Hillebrandt W., Kromer M., Pakmor R., Fink M., Ruiter A. J., Seitenzahl I. R., 2010, ApJ, 714, L52
Sim S. A. et al., 2013, MNRAS, 436, 333
Sullivan M. et al., 2010, MNRAS, 406, 782
Timmes F. X., Brown E. F., Truran J. W., 2003, ApJ, 590, L83
Tinsley B. M., 1979, ApJ, 229, 1046
Townsley D. M., Miles B. J., Shen K. J., Kasen D., 2019, ApJ, 878, L38
van der Walt S., Colbert S. C., Varoquaux G., 2011, Comput. Sci. Eng., 13, 22
Vincenzo F., Spitoni E., Calura F., Matteucci F., Silva Aguirre V., Miglio A., Cescutti G., 2019, MNRAS, 487, L47
Virtanen P. et al., 2020, Nat. Methods, 17, 261
Waskom M. L., 2021, The Open Journal, 6, 3021
Webbink R. F., 1984, ApJ, 277, 355
Weinberg D. H., Andrews B. H., Freudenburg J., 2017, ApJ, 837, 183
Weinberg D. H. et al., 2019, ApJ, 874, 102
Whelan J., Iben Icko J., 1973, ApJ, 186, 1007
Wilson J. C. et al., 2019, PASP, 131, 055001
Woosley S. E., Weaver T. A., 1994, ApJ, 423, 371
Woosley S. E., Weaver T. A., 1995, ApJS, 101, 181
Yan H. L., Shi J. R., Nissen P. E., Zhao G., 2016, A&A, 585, A102

APPENDIX A: COMMON STARS

For the analysis in this paper, it is important that the absolute abundance scale of each data set is well determined, and that the stellar samples are free from systematic trends with stellar parameters (in particular, metallicity). As we have access to multiple data sets we are able to compare abundances for stars observed by two surveys. We initially compare the APOGEE DR16 and GALAH DR3 data sets as they have the largest overlap, and then we go on to compare these data sets with NS10.

A1 APOGEE versus GALAH

We take the same sample of GALAH DR3 as detailed in Section 2.2 without restricting to just *Gaia* Sausage stars, and cross-match to APOGEE DR16 stars with no ASPCAP flags. This results in 479 stars. We fit a series of linear models to the difference in the Mg, Si, Ca, Cr, Mn, Ni, and Cu abundances (only using unflagged abundances) as a function of the stellar parameters ($T_{\rm eff}$, $\log g$, and [Fe/H]). Note that APOGEE Cu is known to be unreliable particularly at low metallicity (Jönsson et al. 2020) so we do not use it in the main body of the paper. We account for the uncertainties in the abundances but not in the stellar parameters (which on the whole are small). Importantly we account for the floor in the APOGEE [X/H] abundances below which abundances are not reported. Excluding this effect biases the trends.

In Table A1, we show the results of fitting linear models to the abundance differences as a function of $T_{\rm eff}$, $\log g$, and [Fe/H] separately, and using all three together. The results of the fits against [Fe/H] are shown in Fig. A1. The results at the metal-rich end are mostly consistent with $\lesssim$0.1 dex difference. Jönsson et al. (2020) show how the majority of APOGEE abundances agree (within $\sim$0.05 dex) in the median with those obtained from optical spectra (using LTE). For Mg and Si we find significant trends with metallicity with APOGEE abundances larger than GALAH at the low-metallicity end. Both of these elements have NLTE corrections in GALAH (Amarsi et al. 2020). Ca also has NLTE corrections in GALAH but we do not observe a trend, just an offset of -0.06 dex. Osorio et al. (2020) found that NLTE corrections for Ca and Mg in the Sun, Arcturus, and Procyon are smaller in the *H*-band than in the optical, and always $\lesssim$0.1 dex. For Cr and Cu, we find a significant trend with APOGEE overestimating relative to GALAH at the metal-poor end. However, Cu in APOGEE is known to be unreliable (Jönsson et al. 2020). For Mn we find essentially no bias between APOGEE and GALAH across the full metallicity range. This is despite the NLTE corrections in GALAH. This gives confidence to the conclusions in the main body of the paper that use the Mn abundances. Finally, with Ni the GALAH analysis used different combinations of the 5847 and 6586 Å lines. We found different trends with respect to the APOGEE Ni abundances when restricting to subsets of GALAH abundances derived from the same combinations. In particular, we found a significant trend when using only 5847 Å whilst no trend for only 6586 Å. This suggests there is a systematic variation in the GALAH Ni abundances.

A2 APOGEE and GALAH versus Nissen & Schuster

We find there are three stars in the NS10 sample also observed as part of GALAH DR3, and nine also observed in APOGEE DR16. In Fig. A2, we plot the difference in the reported abundances and report the inverse-variance-weighted mean difference. Despite the small number of data points, we find good correspondence between the two data sets with only [Cr/Fe] showing a significant offset (GALAH DR3 smaller than NS10). Six of the inspected abundances have 1D NLTE corrections in GALAH DR3 (Amarsi et al. 2020), whilst NS10 use an LTE analysis (except in the case of [Cu/Fe] where we have used the results from Yan et al. 2016).

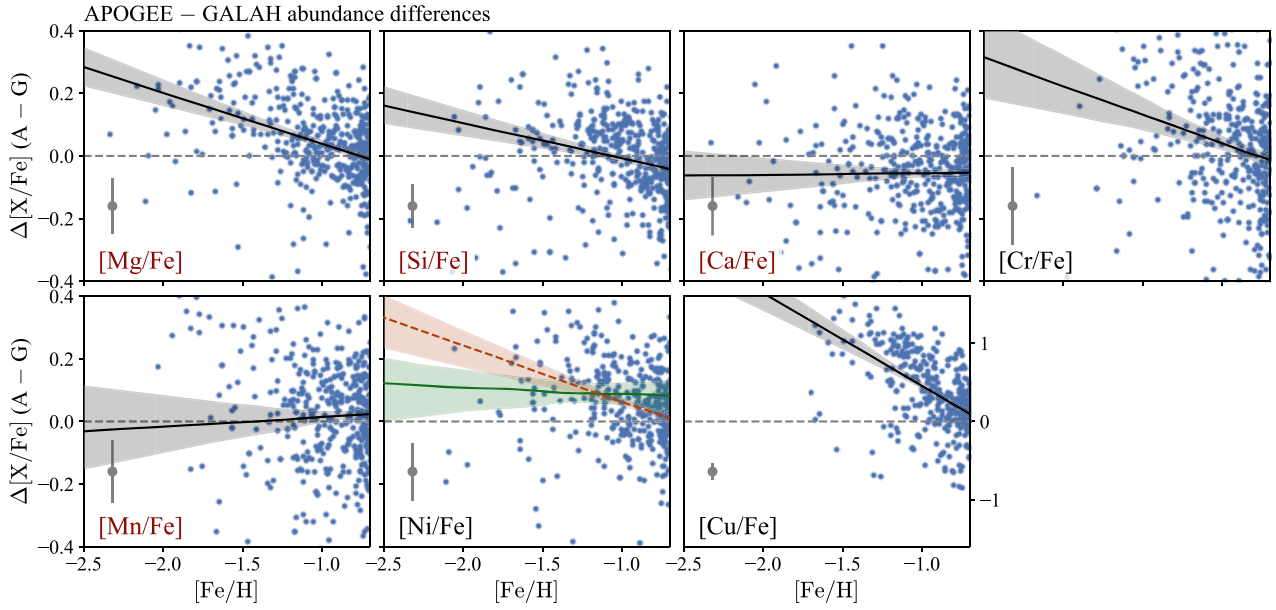

Figure A1. Differences between the APOGEE DR16 and GALAH DR3 abundances plotted against [Fe/H]. Simple linear models are plotted (mostly in black with a 1σ envelope). The parameters of these models are in Table A1. For [Ni/Fe] we show two fits for the GALAH abundances derived from Ni 6586 Å in solid green and for those derived from both Ni 5847 Å and Ni 6586 Å in dashed red. Median errors for the sample are given in the lower left.

Table A1. Offset parameters between common stars observed by APOGEE DR16 and GALAH DR3. Models of the difference between APOGEE and GALAH (i.e. positive numbers mean APOGEE is larger than GALAH) have been fitted with the linear models of the form $c_i + m_{T_{\rm eff}}(T_{\rm eff}/1000\,{\rm K} - 4.5) + m_{\log g}(\log g - 2.5) + m_{\rm [Fe/H]}({\rm [Fe/H]} + 1)$. The top set of fits correspond to a constant model c_0 ($m_{T_{\rm eff}} = m_{\log g} = m_{\rm [Fe/H]} = 0$) and three models where the gradient in only one parameter is fitted for (e.g. $c_{T_{\rm eff}}$, $m_{T_{\rm eff}}$ correspond to the case where ($m_{\log g} = m_{\rm [Fe/H]} = 0$). The second section shows the results for a full multivariate fit. The final section shows the results for fitting a metallicity-dependent model to the Ni differences using the three different line combinations. The spectroscopic parameters ($T_{\rm eff}$, $\log g$, and [Fe/H]) used are those of GALAH DR3, although they differ from APOGEE DR16 parameters by 3.6 K, −0.002 dex, and −0.05 dex in the median.

	c_0	$c_{T_{\rm eff}}$	$m_{T_{\rm eff}}$	$c_{\log g}$	$m_{\log g}$	$c_{\rm [Fe/H]}$	$m_{\rm [Fe/H]}$
Mg	$+0.04^{+0.01}_{-0.01}$	$+0.03^{+0.01}_{-0.01}$	$+0.04^{+0.02}_{-0.02}$	$+0.04^{+0.01}_{-0.01}$	$-0.00^{+0.01}_{-0.01}$	$+0.04^{+0.01}_{-0.01}$	$-0.16^{+0.02}_{-0.02}$
Si	$-0.01^{+0.01}_{-0.01}$	$-0.01^{+0.01}_{-0.01}$	$-0.01^{+0.02}_{-0.02}$	$-0.02^{+0.01}_{-0.01}$	$-0.04^{+0.01}_{-0.01}$	$-0.01^{+0.01}_{-0.01}$	$-0.11^{+0.03}_{-0.03}$
Ca	$-0.05^{+0.01}_{-0.01}$	$-0.06^{+0.01}_{-0.01}$	$+0.04^{+0.02}_{-0.02}$	$-0.04^{+0.01}_{-0.01}$	$+0.03^{+0.01}_{-0.01}$	$-0.06^{+0.01}_{-0.01}$	$+0.01^{+0.03}_{-0.03}$
Cr	$+0.02^{+0.01}_{-0.01}$	$+0.02^{+0.01}_{-0.01}$	$+0.04^{+0.03}_{-0.03}$	$+0.03^{+0.02}_{-0.02}$	$+0.01^{+0.02}_{-0.02}$	$+0.04^{+0.01}_{-0.01}$	$-0.18^{+0.05}_{-0.05}$
Mn	$+0.03^{+0.01}_{-0.01}$	$+0.05^{+0.01}_{-0.01}$	$-0.12^{+0.02}_{-0.02}$	$-0.00^{+0.01}_{-0.01}$	$-0.07^{+0.01}_{-0.01}$	$+0.02^{+0.01}_{-0.01}$	$+0.03^{+0.05}_{-0.05}$
Ni	$+0.06^{+0.01}_{-0.01}$	$+0.04^{+0.01}_{-0.01}$	$+0.11^{+0.02}_{-0.02}$	$+0.07^{+0.01}_{-0.01}$	$+0.02^{+0.01}_{-0.01}$	$+0.06^{+0.01}_{-0.01}$	$-0.13^{+0.03}_{-0.03}$
Cu	$+0.35^{+0.03}_{-0.03}$	$+0.40^{+0.03}_{-0.03}$	$-0.29^{+0.07}_{-0.08}$	$+0.26^{+0.02}_{-0.03}$	$-0.23^{+0.03}_{-0.03}$	$+0.46^{+0.02}_{-0.02}$	$-1.20^{+0.12}_{-0.11}$
Mg	$-0.02^{+0.02}_{-0.02}$	–	$+0.15^{+0.02}_{-0.02}$	–	$-0.07^{+0.02}_{-0.02}$	–	$-0.12^{+0.04}_{-0.03}$
Si	$-0.14^{+0.02}_{-0.02}$	–	$+0.31^{+0.02}_{-0.03}$	–	$-0.17^{+0.02}_{-0.02}$	–	$+0.01^{+0.05}_{-0.04}$
Ca	$-0.02^{+0.01}_{-0.01}$	–	$-0.05^{+0.03}_{-0.03}$	–	$+0.05^{+0.01}_{-0.01}$	–	$-0.04^{+0.03}_{-0.03}$
Cr	$+0.05^{+0.03}_{-0.03}$	–	$-0.03^{+0.06}_{-0.06}$	–	$+0.02^{+0.04}_{-0.04}$	–	$-0.19^{+0.08}_{-0.07}$
Mn	$-0.02^{+0.02}_{-0.02}$	–	$+0.01^{+0.05}_{-0.04}$	–	$-0.07^{+0.02}_{-0.02}$	–	$+0.08^{+0.05}_{-0.05}$
Ni	$+0.05^{+0.01}_{-0.01}$	–	$+0.14^{+0.03}_{-0.03}$	–	$-0.01^{+0.02}_{-0.02}$	–	$-0.14^{+0.04}_{-0.04}$
Cu	$+0.21^{+0.06}_{-0.06}$	–	$+0.62^{+0.11}_{-0.12}$	–	$-0.35^{+0.07}_{-0.06}$	–	$-0.97^{+0.13}_{-0.14}$
Ni 5847 Å	–	–	–	–	–	$+0.02^{+0.09}_{-0.08}$	$+0.29^{+0.36}_{-0.41}$
Ni 6586 Å	–	–	–	–	–	$+0.09^{+0.02}_{-0.02}$	$-0.01^{+0.05}_{-0.05}$
Ni both	–	–	–	–	–	$+0.06^{+0.01}_{-0.01}$	$-0.17^{+0.03}_{-0.03}$

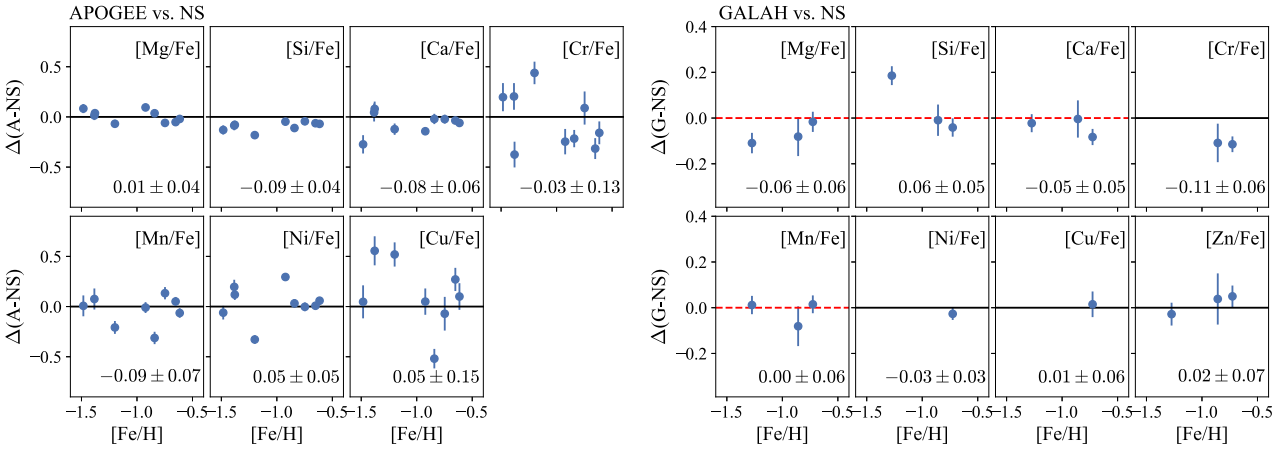

Figure A2. APOGEE DR16 (A, left) and GALAH DR3 (G, right) versus NS10 abundances: we display the difference in abundance measurements for stars in common. The inverse-variance-weighted mean with uncertainty is displayed in each panel. Panels with red dashed horizontal lines have 1D NLTE corrections applied in GALAH. Note the different scales for the left- and right-hand sets of panels.

APPENDIX B: AUXILIARY DATA TABLES

Here we provide additional data tables from out study. The results using the exponential star formation rate of Weinberg et al. (2017) applied to the NS10 data are shown in Table B1. The full set of constrained parameters for the Local Group systems are shown in Table B2. We show the corresponding models for the most massive five systems (*Gaia* Sausage, Sgr, SMC, LMC, and the MW bulge) in Fig. B1.

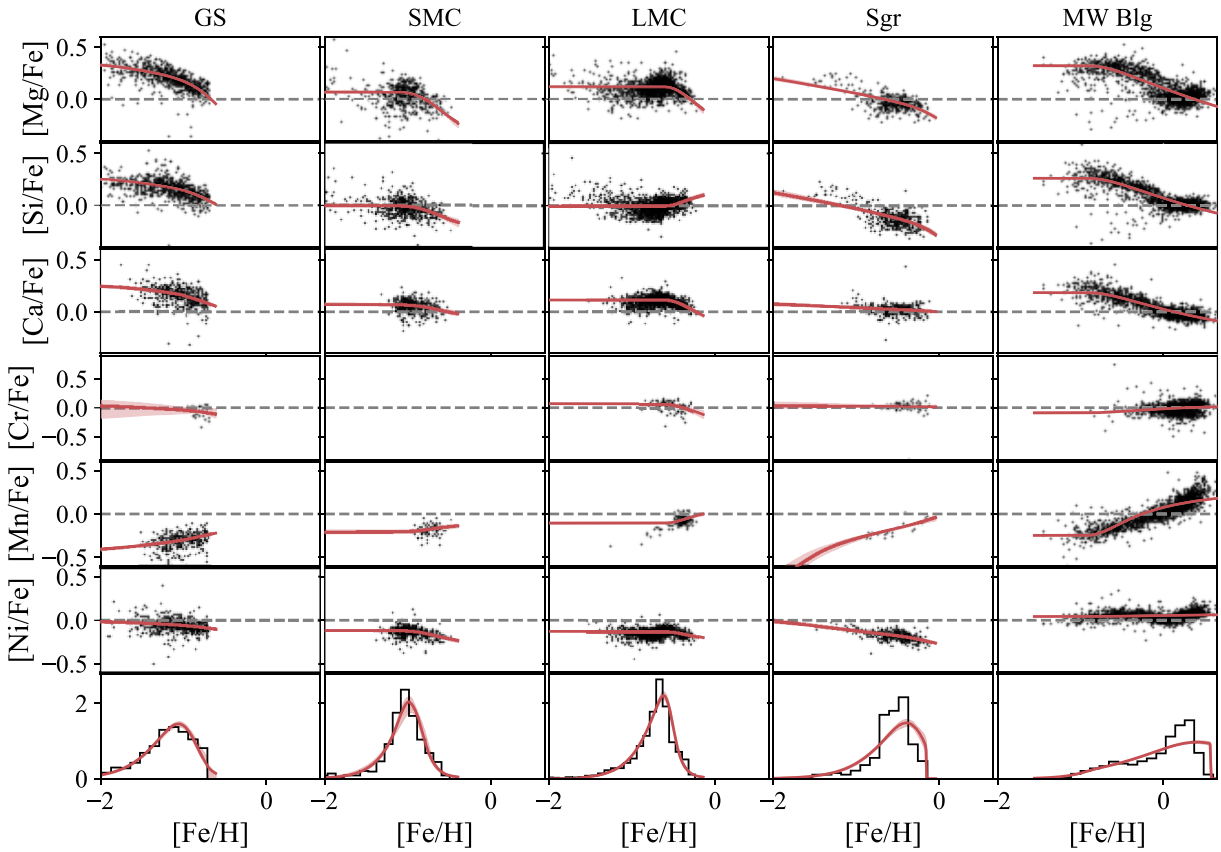

Figure B1. Chemical evolution model fits for *Gaia* Sausage, SMC, LMC, Sgr, and the MW bulge. The data for each abundance [X/Fe] versus metallicity are shown in black with the bottom row showing the metallicity distribution of the data. The red lines show the median model fits and the bands the 16th and 84th percentile confidence interval.

Table B1. Comparison between derived yields using Nissen & Schuster (2010) data set with linear–exponential star formation model (NS10) and the exponential model (NS10 Exp Model) as detailed by Weinberg et al. (2017).

Type	Element	NS10	NS10 Exp Model
Ia	$\log_{10} m_{\rm Fe}$	$-2.73^{+0.10}_{-0.10}$	$-2.77^{+0.10}_{-0.10}$
Ia	[Mg/Fe]	$-2.00^{+0.35}_{-0.34}$	$-1.99^{+0.33}_{-0.34}$
Ia	[Si/Fe]	$-0.87^{+0.34}_{-0.54}$	$-0.85^{+0.34}_{-0.52}$
Ia	[Ca/Fe]	$-0.72^{+0.31}_{-0.52}$	$-0.68^{+0.29}_{-0.50}$
Ia	[Cr/Fe]	$+0.03^{+0.03}_{-0.03}$	$+0.02^{+0.03}_{-0.03}$
Ia	[Mn/Fe]	$-0.16^{+0.03}_{-0.03}$	$-0.17^{+0.03}_{-0.03}$
Ia	[Ni/Fe]	$-0.41^{+0.08}_{-0.12}$	$-0.41^{+0.08}_{-0.11}$
Ia	[Cu/Fe]	$-0.46^{+0.19}_{-0.35}$	$-0.49^{+0.21}_{-0.35}$
Ia	[Zn/Fe]	$-0.91^{+0.31}_{-0.52}$	$-0.90^{+0.31}_{-0.49}$
II	$\log_{10} m_{\rm Fe}$	$-3.08^{+0.16}_{-0.16}$	$-2.93^{+0.14}_{-0.15}$
II	[Mg/Fe]	$+0.48^{+0.11}_{-0.09}$	$+0.41^{+0.09}_{-0.07}$
II	[Si/Fe]	$+0.46^{+0.10}_{-0.09}$	$+0.40^{+0.09}_{-0.06}$
II	[Ca/Fe]	$+0.54^{+0.10}_{-0.08}$	$+0.47^{+0.09}_{-0.06}$
II	[Cr/Fe]	$-0.07^{+0.04}_{-0.06}$	$-0.05^{+0.02}_{-0.04}$
II	[Mn/Fe]	$-0.56^{+0.11}_{-0.27}$	$-0.47^{+0.06}_{-0.14}$
II	[Ni/Fe]	$+0.08^{+0.08}_{-0.06}$	$+0.03^{+0.07}_{-0.04}$
II	[Cu/Fe]	$-0.41^{+0.19}_{-0.35}$	$-0.39^{+0.14}_{-0.23}$
II	[Zn/Fe]	$+0.29^{+0.10}_{-0.08}$	$+0.22^{+0.09}_{-0.06}$

Table B2. Type Ia and Type II supernovae abundances and evolutionary parameters for chemical evolution models fitted to a range of Local Group systems. We give the median metallicity of the stars used to model each system.

Type	Element	UMi	CVnI	Leo I	Scl	GS	For	SMC	LMC	Sgr	MW blg
	[Fe/H]	-2.21	-1.98	-1.43	-1.63	-1.17	-1.07	-1.04	-0.69	-0.53	0.08
Ia	$\log_{10} m_{\rm Fe}$	$-2.91^{+0.08}_{-0.08}$	$-2.80^{+0.09}_{-0.09}$	$-2.76^{+0.09}_{-0.10}$	$-2.65^{+0.09}_{-0.09}$	$-2.85^{+0.09}_{-0.09}$	$-2.89^{+0.09}_{-0.10}$	$-2.93^{+0.09}_{-0.09}$	$-2.99^{+0.10}_{-0.10}$	$-2.78^{+0.11}_{-0.10}$	$-2.30^{+0.05}_{-0.08}$
Ia	[Mg/Fe]	$-2.01^{+0.33}_{-0.35}$	$-2.00^{+0.33}_{-0.34}$	$-2.02^{+0.33}_{-0.34}$	$-2.02^{+0.34}_{-0.33}$	$-1.97^{+0.37}_{-0.36}$	$-1.98^{+0.37}_{-0.35}$	$-0.60^{+0.08}_{-1.29}$	$-0.58^{+0.06}_{-0.64}$	$-1.29^{+0.72}_{-0.72}$	$-0.507^{+0.006}_{-0.013}$
Ia	[Si/Fe]	$-0.22^{+0.18}_{-0.29}$	$-1.04^{+0.45}_{-0.56}$	$-1.05^{+0.34}_{-0.48}$	$-1.36^{+0.35}_{-0.48}$	$-0.32^{+0.05}_{-0.06}$	$-0.30^{+0.17}_{-0.25}$	$-0.29^{+0.06}_{-0.13}$	$+0.19^{+0.02}_{-0.02}$	$-1.44^{+0.49}_{-0.49}$	$-0.38^{+0.02}_{-0.02}$
Ia	[Ca/Fe]	$-0.31^{+0.18}_{-0.36}$	$-0.36^{+0.21}_{-0.44}$	$-0.19^{+0.05}_{-0.07}$	$-0.23^{+0.05}_{-0.05}$	$-0.17^{+0.05}_{-0.06}$	$-0.55^{+0.29}_{-0.48}$	$-0.07^{+0.03}_{-0.06}$	$-0.28^{+0.05}_{-0.08}$	$-0.05^{+0.02}_{-0.03}$	$-0.29^{+0.01}_{-0.01}$
Ia	[Cr/Fe]	$-1.04^{+0.39}_{-0.56}$	$-0.01^{+0.15}_{-0.42}$	$+0.63^{+0.05}_{-0.04}$	$+0.00^{+0.03}_{-0.03}$	$-0.23^{+0.31}_{-0.55}$	$+0.65^{+0.10}_{-0.09}$	$-0.01^{+0.83}_{-0.83}$	$-0.53^{+0.28}_{-0.49}$	$+0.00^{+0.07}_{-0.07}$	$+0.054^{+0.009}_{-0.009}$
Ia	[Mn/Fe]	$-0.44^{+0.22}_{-0.39}$	$-0.29^{+0.19}_{-0.36}$	$-0.20^{+0.11}_{-0.14}$	$-0.38^{+0.06}_{-0.07}$	$-0.12^{+0.02}_{-0.02}$	$-0.17^{+0.24}_{-0.42}$	$-0.09^{+0.04}_{-0.04}$	$+0.09^{+0.03}_{-0.03}$	$+0.13^{+0.05}_{-0.05}$	$+0.284^{+0.005}_{-0.005}$
Ia	[Ni/Fe]	$-0.91^{+0.44}_{-0.53}$	$-0.47^{+0.12}_{-0.28}$	$+0.11^{+0.03}_{-0.03}$	$-0.29^{+0.02}_{-0.02}$	$-0.18^{+0.02}_{-0.02}$	$+0.36^{+0.07}_{-0.07}$	$-0.32^{+0.03}_{-0.08}$	$-0.29^{+0.02}_{-0.03}$	$-0.54^{+0.09}_{-0.09}$	$+0.071^{+0.003}_{-0.003}$
II	$\log_{10} m_{\rm Fe}$	$-3.15^{+0.11}_{-0.12}$	$-3.31^{+0.14}_{-0.16}$	$-3.05^{+0.13}_{-0.11}$	$-3.42^{+0.10}_{-0.10}$	$-2.70^{+0.09}_{-0.09}$	$-2.54^{+0.12}_{-0.13}$	$-2.42^{+0.11}_{-0.12}$	$-2.22^{+0.10}_{-0.11}$	$-2.92^{+0.11}_{-0.12}$	$-3.01^{+0.04}_{-0.04}$
II	[Mg/Fe]	$+0.80^{+0.10}_{-0.09}$	$+0.77^{+0.22}_{-0.20}$	$+0.64^{+0.07}_{-0.06}$	$+0.75^{+0.06}_{-0.05}$	$+0.34^{+0.02}_{-0.02}$	$+0.22^{+0.04}_{-0.03}$	$+0.067^{+0.026}_{-0.006}$	$+0.120^{+0.002}_{-0.002}$	$+0.23^{+0.04}_{-0.03}$	$+0.322^{+0.004}_{-0.004}$
II	[Si/Fe]	$+0.57^{+0.07}_{-0.06}$	$+0.60^{+0.14}_{-0.13}$	$+0.42^{+0.07}_{-0.06}$	$+0.64^{+0.05}_{-0.05}$	$+0.26^{+0.01}_{-0.01}$	$+0.07^{+0.04}_{-0.03}$	$-0.004^{+0.018}_{-0.004}$	$-0.002^{+0.002}_{-0.002}$	$+0.15^{+0.04}_{-0.03}$	$+0.261^{+0.004}_{-0.004}$
II	[Ca/Fe]	$+0.31^{+0.05}_{-0.04}$	$+0.29^{+0.13}_{-0.12}$	$+0.16^{+0.04}_{-0.04}$	$+0.48^{+0.04}_{-0.04}$	$+0.25^{+0.02}_{-0.01}$	$+0.06^{+0.04}_{-0.04}$	$+0.070^{+0.011}_{-0.005}$	$+0.113^{+0.001}_{-0.001}$	$+0.08^{+0.02}_{-0.02}$	$+0.184^{+0.003}_{-0.003}$
II	[Cr/Fe]	$+0.32^{+0.09}_{-0.08}$	$+0.04^{+0.41}_{-0.73}$	$-0.56^{+0.33}_{-0.62}$	$-0.13^{+0.09}_{-0.10}$	$+0.03^{+0.11}_{-0.24}$	$-0.09^{+0.11}_{-0.17}$	$-0.04^{+0.86}_{-0.84}$	$+0.07^{+0.01}_{-0.01}$	$+0.05^{+0.06}_{-0.08}$	$-0.09^{+0.01}_{-0.01}$
II	[Mn/Fe]	$-0.15^{+0.14}_{-0.15}$	$-0.20^{+0.26}_{-0.44}$	$-0.07^{+0.13}_{-0.15}$	$-0.29^{+0.10}_{-0.12}$	$-0.42^{+0.02}_{-0.03}$	$-0.07^{+0.07}_{-0.09}$	$-0.21^{+0.02}_{-0.02}$	$-0.11^{+0.01}_{-0.01}$	$-1.26^{+0.38}_{-0.52}$	$-0.248^{+0.007}_{-0.007}$
II	[Ni/Fe]	$+0.03^{+0.05}_{-0.05}$	$+0.03^{+0.12}_{-0.10}$	$-0.11^{+0.04}_{-0.05}$	$-0.00^{+0.03}_{-0.03}$	$-0.012^{+0.009}_{-0.008}$	$-0.26^{+0.04}_{-0.06}$	$-0.118^{+0.014}_{-0.003}$	$-0.128^{+0.001}_{-0.001}$	$+0.01^{+0.03}_{-0.02}$	$+0.042^{+0.003}_{-0.003}$
$\tau_{\rm sfh}$		$0.46^{+0.12}_{-0.13}$	$2.25^{+1.46}_{-0.80}$	$2.88^{+0.28}_{-0.31}$	$0.97^{+0.17}_{-0.17}$	$0.79^{+0.23}_{-0.14}$	$2.31^{+0.33}_{-0.31}$	$0.27^{+0.57}_{-0.05}$	$0.14^{+0.02}_{-0.02}$	$2.10^{+0.31}_{-0.31}$	$0.82^{+0.16}_{-0.15}$
$t_{\rm max}$		$4.68^{+0.91}_{-0.91}$	$10.09^{+1.87}_{-1.95}$	$13.01^{+0.72}_{-1.26}$	$3.77^{+0.79}_{-0.74}$	$5.25^{+0.86}_{-0.95}$	$13.01^{+0.70}_{-1.31}$	$9.50^{+3.17}_{-1.94}$	$3.17^{+0.61}_{-0.50}$	$7.33^{+1.24}_{-1.26}$	$1.83^{+0.33}_{-0.33}$
$\tau_\star$		$26.43^{+14.58}_{-10.37}$	$88.05^{+81.16}_{-52.68}$	$23.70^{+8.47}_{-6.93}$	$13.52^{+5.66}_{-4.11}$	$14.06^{+4.96}_{-3.34}$	$23.19^{+8.78}_{-6.51}$	$4.35^{+15.42}_{-1.54}$	$1.89^{+0.74}_{-0.53}$	$7.56^{+2.46}_{-1.93}$	$0.75^{+0.20}_{-0.14}$
η		$138.65^{+27.01}_{-24.02}$	$99.88^{+27.59}_{-29.33}$	$47.05^{+11.84}_{-8.83}$	$42.04^{+10.76}_{-8.89}$	$28.82^{+6.92}_{-5.97}$	$32.74^{+9.14}_{-7.32}$	$33.62^{+11.00}_{-8.38}$	$23.48^{+6.39}_{-5.37}$	$4.84^{+1.46}_{-1.29}$	$0.03^{+0.04}_{-0.02}$
$\tau_{\rm dep}$		$0.19^{+0.09}_{-0.07}$	$0.81^{+1.37}_{-0.48}$	$0.50^{+0.11}_{-0.11}$	$0.32^{+0.08}_{-0.07}$	$0.47^{+0.15}_{-0.08}$	$0.70^{+0.15}_{-0.12}$	$0.13^{+0.35}_{-0.03}$	$0.08^{+0.01}_{-0.01}$	$1.38^{+0.36}_{-0.25}$	$1.18^{+0.30}_{-0.23}$
$t_{\rm D}$		$0.13^{+0.05}_{-0.05}$	$0.17^{+0.05}_{-0.04}$	$0.20^{+0.04}_{-0.04}$	$0.21^{+0.04}_{-0.04}$	$0.07^{+0.08}_{-0.02}$	$0.16^{+0.05}_{-0.05}$	$0.25^{+0.05}_{-0.15}$	$0.26^{+0.04}_{-0.04}$	$0.048^{+0.013}_{-0.006}$	$0.21^{+0.04}_{-0.04}$
$f_{\rm mix}$		$0.97^{+0.02}_{-0.03}$	$0.97^{+0.02}_{-0.03}$	$0.990^{+0.007}_{-0.015}$	$0.976^{+0.009}_{-0.012}$	$0.92^{+0.02}_{-0.02}$	$0.989^{+0.008}_{-0.019}$	$0.91^{+0.02}_{-0.02}$	$0.958^{+0.009}_{-0.011}$	$0.985^{+0.006}_{-0.010}$	$0.936^{+0.007}_{-0.006}$

This paper has been typeset from a TEX/LATEX file prepared by the author.